

Atmospheric effects of the total solar eclipse of 4 December 2002 simulated with a high-altitude global model

S. D. Eckermann,¹ D. Broutman,² M. T. Stollberg,³ J. Ma,² J. P. McCormack,¹ and T. F. Hogan⁴

Received 3 August 2006; revised 3 March 2007; accepted 10 May 2007; published 25 July 2007.

[1] The atmosphere's response to the total solar eclipse of 4 December 2002 is studied using a prototype high-altitude global numerical weather prediction model (NOGAPS-ALPHA). Local reductions in solar ultraviolet (UV) radiation during the eclipse are estimated using astronomical calculations of umbral and penumbral surface trajectories and observed solar limb darkening at $\sim 200\text{--}300$ nm. In NOGAPS-ALPHA these UV eclipse shadows yield stratospheric radiative cooling rate footprints peaking near 27 K day^{-1} , a value 2–3 times larger than assumed in previous modeling. Difference fields between NOGAPS-ALPHA runs with and without this eclipse forcing reveal vertically deep middle atmospheric responses, with three-dimensional horizontal structures very similar to the large-scale “bow-wave” response first proposed by Chimonas (1970). Such structure appears clearly only at later times when total eclipses have abated and gravity waves generated in the stratosphere have had time to propagate vertically. Bow-wave amplitudes and direct thermal cooling responses are both small ($\lesssim 1\text{ K}$ for temperature and $\lesssim 2\text{--}3\text{ m s}^{-1}$ for horizontal winds), contradicting some rocketsonde measurements that suggest much larger responses near 50–60 km altitude. We also find clear evidence of a bow-wave-like response in the model's surface pressure fields, with an amplitude $\sim 0.1\text{--}0.5\text{ hPa}$, while surface air temperatures in NOGAPS-ALPHA show $\sim 4\text{ K}$ cooling over Africa during the eclipse. Both findings are consistent with surface atmospheric data acquired during previous eclipse passages.

Citation: Eckermann, S. D., D. Broutman, M. T. Stollberg, J. Ma, J. P. McCormack, and T. F. Hogan (2007), Atmospheric effects of the total solar eclipse of 4 December 2002 simulated with a high-altitude global model, *J. Geophys. Res.*, *112*, D14105, doi:10.1029/2006JD007880.

1. Introduction

[2] Solar eclipses provide natural predictable perturbation experiments for studying the atmosphere's response to changes in solar forcing. From the earliest days of atmospheric research, meteorological measurements have been stationed within predicted paths of eclipse shadows to investigate these sensitivities (for a brief historical review, see *Aplin and Harrison* [2003, section 2]). In the middle atmosphere, the earliest such measurements focused on ozone changes during eclipses, given evolving understanding of the role of solar ultraviolet photolysis in odd oxygen production in the stratosphere and mesosphere [*Kawabata*, 1937; *Jerlov et al.*, 1954; *Stranz*, 1961; *Hunt*, 1965;

Randhawa, 1968]. Rocketsonde sounding experiments also searched for eclipse-related changes to stratospheric and mesospheric winds and temperatures [*Ballard et al.*, 1969].

[3] These exploratory measurements were given greater impetus and focus by the theoretical study of *Chimonas* [1970]. Modeling the eclipse shadow as a moving three-dimensional cooling rate perturbation to the stratosphere due to reduced shortwave ozone heating, *Chimonas* [1970] solved the perturbation fluid equations to infer the atmosphere's response to this diabatic forcing. His solutions predicted a long-wavelength three-dimensional bow-wave-like gravity wave in the wake of the moving eclipse shadow, which propagated vertically to both higher and lower altitudes.

[4] Just prior to the total solar eclipse of 7 March 1970, *Chimonas and Hines* [1970] used the predicted path of the surface eclipse shadow and formulas from *Chimonas* [1970] to predict geographical regions where the hypothetical bow wave response might be observed, both near the ground and in the ionosphere. After the event, *Chimonas and Hines* [1971] argued that traveling ionospheric disturbances (TIDs) measured remotely by *Davis and da Rosa* [1970] from a ground location in the path of the eclipse shadow

¹Space Science Division, Naval Research Laboratory, Washington, D. C., USA.

²Computational Physics, Inc., Springfield, Virginia, USA.

³Astronomical Applications Department, U.S. Naval Observatory, Washington, D. C., USA.

⁴Marine Meteorology Division, Naval Research Laboratory, Monterey, California, USA.

Report Documentation Page				Form Approved OMB No. 0704-0188	
Public reporting burden for the collection of information is estimated to average 1 hour per response, including the time for reviewing instructions, searching existing data sources, gathering and maintaining the data needed, and completing and reviewing the collection of information. Send comments regarding this burden estimate or any other aspect of this collection of information, including suggestions for reducing this burden, to Washington Headquarters Services, Directorate for Information Operations and Reports, 1215 Jefferson Davis Highway, Suite 1204, Arlington VA 22202-4302. Respondents should be aware that notwithstanding any other provision of law, no person shall be subject to a penalty for failing to comply with a collection of information if it does not display a currently valid OMB control number.					
1. REPORT DATE 2007		2. REPORT TYPE		3. DATES COVERED 00-00-2007 to 00-00-2007	
4. TITLE AND SUBTITLE Atmospheric effects of the total solar eclipse of 4 December 2002 simulated with a high-altitude global model				5a. CONTRACT NUMBER	
				5b. GRANT NUMBER	
				5c. PROGRAM ELEMENT NUMBER	
6. AUTHOR(S)				5d. PROJECT NUMBER	
				5e. TASK NUMBER	
				5f. WORK UNIT NUMBER	
7. PERFORMING ORGANIZATION NAME(S) AND ADDRESS(ES) Naval Research Laboratory,Space Science Division,4555 Overlook Avenue SW,Washington,DC,20375				8. PERFORMING ORGANIZATION REPORT NUMBER	
9. SPONSORING/MONITORING AGENCY NAME(S) AND ADDRESS(ES)				10. SPONSOR/MONITOR'S ACRONYM(S)	
				11. SPONSOR/MONITOR'S REPORT NUMBER(S)	
12. DISTRIBUTION/AVAILABILITY STATEMENT Approved for public release; distribution unlimited					
13. SUPPLEMENTARY NOTES					
14. ABSTRACT					
15. SUBJECT TERMS					
16. SECURITY CLASSIFICATION OF:			17. LIMITATION OF ABSTRACT 7	18. NUMBER OF PAGES 22	19a. NAME OF RESPONSIBLE PERSON
a. REPORT unclassified	b. ABSTRACT unclassified	c. THIS PAGE unclassified			

directly validated their predictions. However, more detailed postanalyses of the TIDs observed by *Davis and da Rosa* [1970] and others led to a consensus that the source could not be definitively ascribed to the eclipse: one of the many other sources of TIDs, such as the strong magnetic storm activity that occurred at the time, could just as easily have generated these waves [see, e.g., *Sears*, 1972; *Arendt*, 1972; *Schödel et al.*, 1973; *Frost and Clark*, 1973]. Near the surface, *Anderson et al.* [1972] measured atmospheric pressure oscillations qualitatively similar to those predicted by *Chimonas and Hines* [1970], but with amplitudes 1–2 orders of magnitude larger. They reported similar features in other surface pressure measurements during eclipses, extending back to the turn of the century. This led *Chimonas* [1973] to propose a completely different theory for these observations, in terms of a Lamb wave driven by net radiative cooling of tropospheric cloud layers. Recent modeling has suggested that in situ generation of atmospheric waves by eclipses can also occur in the thermosphere [*Müller-Wodarg et al.*, 1998], because of reduced heating by absorption of extreme ultraviolet solar radiation.

[5] These source ambiguities have complicated subsequent experimental studies that have sought evidence of eclipse-generated gravity waves. In the upper atmosphere, some observers report null detections [e.g., *Schödel et al.*, 1973; *Hunter et al.*, 1974; *Boitman et al.*, 1999], whereas others find oscillations apparently consistent with an eclipse-generated gravity wave, but disagree on whether the source is stratospheric or thermospheric [e.g., *Bertin et al.*, 1977; *Hanuse et al.*, 1982; *Altadil et al.*, 2001; *Farges et al.*, 2003; *Jones et al.*, 2004]. Similarly, some studies of near-surface pressure observations present evidence of eclipse-related wave oscillations, but disagree as to the eclipse-mediated source mechanism [e.g., *Goodwin and Hobson*, 1978; *McIntosh and Revelle*, 1984; *Seykora et al.*, 1985; *Farges et al.*, 2003], while others report null detections [e.g., *Jones and Bogart*, 1975; *Anderson and Keefer*, 1975; *Jones*, 1976, 1999]. On collating results from those studies reporting positive wave detections, both in the lower and upper atmospheres, a wide spread of inferred wave properties is revealed [see, e.g., *Farges et al.*, 2003]. These facts led *Davies* [1982] to question whether any definitive experimental evidence exists for a characteristic eclipse-generated gravity wave due to reduced ozone heating in the stratosphere.

[6] Direct upper stratospheric or mesospheric measurements could help to clarify this situation, but far fewer measurements exist at these altitudes because of the difficulties in acquiring high-resolution day-night data. Some limited rocketsonde measurements have shown surprisingly large temperature decreases and associated meridional wind changes in the lower mesosphere during eclipses [*Ballard et al.*, 1969; *Quiroz and Henry*, 1973; *Randhawa*, 1974; *Schmidlin and Olsen*, 1984], whereas other measurements have found no discernable changes [*Randhawa*, 1973; *Ball et al.*, 1980].

[7] In summary, despite decades of research, observational evidence for a characteristic bow-wave response of the atmosphere to eclipse passages remains equivocal. One issue could be the simplicity of existing models. For example, the only extension to the analytical *Chimonas* [1970] theory was provided by *Fritts and Luo* [1993], who

derived numerical solutions to the pseudo-incompressible perturbation equations using approximations for thermal eclipse forcing, shadow speed and background atmospheric conditions similar to those used by *Chimonas* [1970]. *Jones* [1999] has argued for more realistic model predictions for specific eclipse events to help guide future observations. Several thermospheric general circulation models (GCMs) have simulated the upper atmosphere's response to eclipses, finding strong in situ temperature, wind and composition changes peaking at ~ 250 – 300 km altitude [*Ridley et al.*, 1984; *Roble et al.*, 1986; *Müller-Wodarg et al.*, 1998]. Since their lower boundaries were all ≥ 80 km, these models did not simulate stratospheric ozone cooling due to the eclipse and thus could not simulate the specific bow waves predicted by *Chimonas* [1970] and *Fritts and Luo* [1993]. Several mesoscale weather models have simulated regional changes in near-surface conditions associated with eclipse passages [*Gross and Hense*, 1999; *Prenosil*, 2000; *Vogel et al.*, 2001]. These models do not extend through the stratosphere and lack the global scale needed to simulate the fast-moving large-scale gravity wave and Lamb wave responses anticipated by *Chimonas* [1970, 1973].

[8] In this paper, we use a state-of-the-art global numerical weather prediction (NWP) model that, as described in section 3, contains the necessary physics to simulate realistic time-dependent thermal cooling of the troposphere and stratosphere during a solar eclipse. In section 2 we use precomputed time histories of the lunar shadow's motion across the Southern Hemisphere during the total solar eclipse of 4 December 2002 to specify corresponding reductions in solar ultraviolet insolation during the eclipse. In section 4, difference fields between model hindcasts run with and without these eclipse effects included are used to isolate the model's simulated response to this eclipse. In section 5 we compare these responses to the predictions of stratospheric bow wave theory, tropospheric Lamb wave theory, and relevant observations. Major findings are summarized in section 6.

2. Total Solar Eclipse of 4 December 2002

[9] Detailed calculations of solar eclipse properties are issued ahead of time by the U.S. Naval Observatory (USNO). Figure 1a characterizes properties of the 4 December 2002 total eclipse from USNO calculations. Gray curves show 30 s time series of the southern and northern limits of the penumbral (partial) and umbral (total) eclipse shadows, the latter showing the very small geographical size of the total eclipse regions at any given time.

[10] Standard USNO eclipse calculations also include 30 min time series of the leading and lagging limbs of the lunar shadow on the Earth, which define the geographical perimeter of the eclipse penumbra. For this study, those calculations were repeated to increase the density of those fields to 1 min. However, these calculations do not currently provide the geographical distribution of eclipse magnitudes E_M within the penumbral region. Appendix A describes the calculations we performed to estimate time-varying eclipse magnitudes E_M over the Earth's surface, and to convert them into a corresponding reduction factor for the total incoming UV solar irradiance, E_{UV} , hereafter called the UV obscuration.

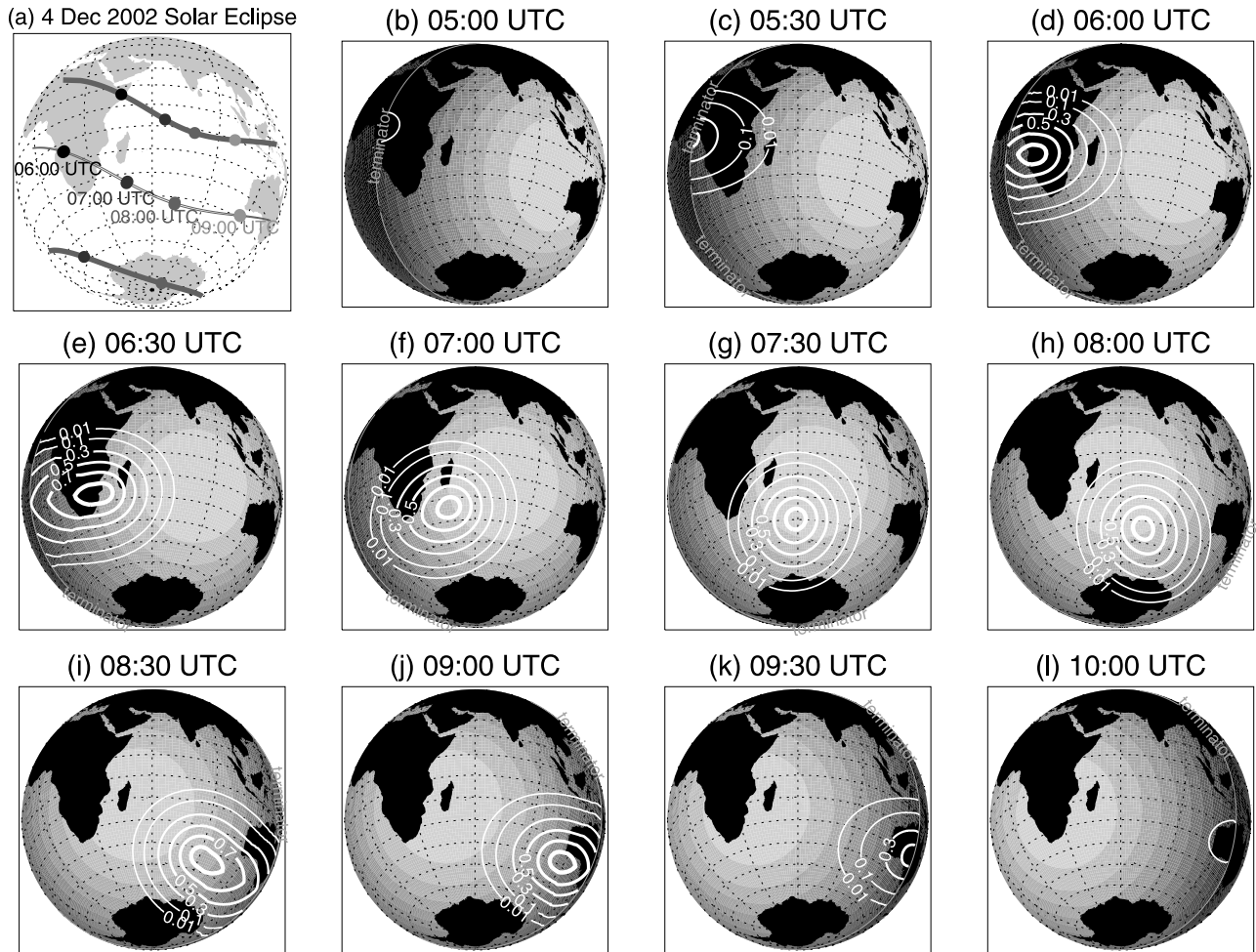


Figure 1. (a) Properties of the 4 December 2002 solar eclipse. Thick gray curves show northernmost and southernmost limits of eclipse penumbra (partial eclipse), thin gray curve shows ground track of the eclipse umbra (total eclipse). Solid circles show points every hour along these curves from 0600 UTC to 0900 UTC. (b–l) White contours show eclipse UV obscurations, E_{UV} , at 30 min intervals from 0500 UTC to 1000 UTC. Contour levels are 0.01, 0.1, 0.3, 0.5, 0.7 and 0.9. Gray shading shows cosines of local solar zenith angles ϕ at $\cos \phi$ intervals of 0.1. The terminator ($\cos \phi = 0$) is labeled in each plot. A color animation of the time sequence in Figures 1b–1l is provided as auxiliary material.

[11] Figures 1b–1l plot these USNO-based E_{UV} estimates every 30 min during the eclipse, along with contours of $\cos \phi$, where ϕ is the solar zenith angle. Animation S1¹ provides a color version of this same presentation at 2 min resolution for the entire period of the eclipse, depicting both the time evolution and speed of passage of these E_{UV} contours across the globe. At 0500 UTC and 0530 UTC, partial eclipsing of the Sun commences over Africa during early morning hours, and by 0600 UTC regions of totality form over parts of Africa. From 0700 to 0800 UTC the penumbral perimeter closes and the total eclipse regions move rapidly eastward across the Southern Ocean at local times near midday ($\cos \phi \sim 1$). Total eclipses persist to 0900 UTC, then the remaining partial eclipse regions shrink and eventually disappear with the setting Sun over Australia just after 1000 UTC.

¹Auxiliary materials are available in the HTML. doi:10.1029/2006JD007880.

[12] Figure 2 plots the speed of the umbral shadow, \bar{V} , across the surface of the Earth. The umbral footprint moves very rapidly to the east at the start and end times of total eclipse in regions where local solar zenith angles are large and the Sun is low in the sky (see, e.g., Figure 1d). Umbral motion reaches a minimum speed of $\sim 700 \text{ m s}^{-1}$ near 0730 UTC over the Southern Ocean between Africa and Australia when the Sun is much higher in the sky (see Figure 1g).

3. Modeling Tools

3.1. NOGAPS-ALPHA

[13] The Navy Operational Global Atmospheric Prediction System (NOGAPS) is the Department of Defense's (DoD) global numerical weather prediction system [Hogan and Rosmond, 1991]. Here we use a prototype advanced-level physics high-altitude (ALPHA) version of the NOGAPS global spectral forecast model component, referred to as

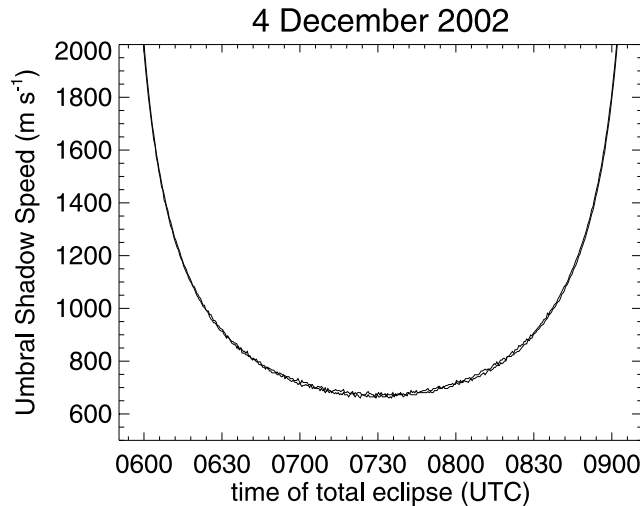


Figure 2. Speed \bar{V} of the umbral shadow as a function of universal time for the total solar eclipse of 4 December 2002.

NOGAPS-ALPHA. Complete descriptions of NOGAPS-ALPHA are provided by Eckermann *et al.* [2004] and Allen *et al.* [2006]. We focus here only on those components salient to the eclipse simulations reported here.

3.1.1. Radiation

3.1.1.1. Standard Model

[14] NOGAPS-ALPHA currently uses the so-called CLIRAD (climate radiation) radiative heating and cooling rate parameterizations of Chou and Suarez [1999] and Chou *et al.* [2001], respectively. As implemented in NOGAPS-ALPHA, the Chou and Suarez [1999] scheme calculates the absorption of ultraviolet, visible and infrared solar radiation by O_3 , O_2 , CO_2 , water vapor and both convective and stable clouds, as well as Rayleigh, surface and cloud scattering. At the surface, model albedos are used to compute the direct and diffuse infrared, visible and ultraviolet fluxes. We use a solar constant S_0 with a base value of 1365 W m^{-2} that then varies with the Earth's orbital position according to Paltridge and Platt [1976, equation (3.3)]. The Chou *et al.* [2001] longwave cooling scheme computes transmission and absorption by O_3 , CO_2 , water vapor and clouds, as well as cloud scattering. Both schemes yield heating and cooling rates accurate to within 5% of line-by-line calculations from the ground to 0.01 hPa.

[15] The radiation schemes use NOGAPS-ALPHA's prognostic specific humidity and cloud fields between the surface and 100 hPa. At altitudes above 100 hPa, specific humidities are set in the radiation schemes by zonal-mean climatologies that vary as a function of month, latitude and pressure, which are interpolated to the day of year and location of the grid point in question. The climatology is based on multiyear version 18 Halogen Occultation Experiment (HALOE) data [Jackson *et al.*, 1998] from 100 to 0.3 hPa, and diurnally averaged output from the CHEM2D model [McCormack and Siskind, 2002] from 0.3 to 0.001 hPa.

[16] While NOGAPS-ALPHA has a prognostic ozone capability [McCormack *et al.*, 2004], for the runs reported here we specified ozone for the radiation calculations using

a zonal-mean observational climatology that varies with month, latitude and pressure, which is then interpolated to the specific day of year, pressure and latitude of each model grid box. The climatology used here is an amalgam from various sources: (1) the Fortuin and Kelder [1998] climatology (1000–200 hPa), (2) the 11-year HALOE climatology of Grooss and Russell [2005] (150–0.1 hPa), and (3) zonal-mean values from the four-dimensional ozone climatology of the United Kingdom (UK) Universities Global Atmospheric Modelling Project (UGAMP) [Li and Shine, 1995] (0.1–0.001 hPa). The resulting ozone mixing ratios for December are plotted in Figure 3a. The values above the 1 hPa level are daytime averages only, mainly data from the Solar Mesosphere Explorer in the case of the UGAMP climatology [Li and Shine, 1995], and compare favorably with more recent satellite measurements of daytime ozone in the upper stratosphere and mesosphere [e.g., Ricard *et al.*, 1996; Kaufmann *et al.*, 2003]. These ozone mixing ratios are used for the daytime heating and cooling rate calculations.

[17] For the nighttime cooling rate calculations, these mixing ratios are scaled by the night-to-day profile in Figure 3b, which is based on one-dimensional photochemical model calculations [Siskind *et al.*, 1995]. Use of a single profile reflects the fact that the magnitude of the diurnal ozone variation in the upper stratosphere and lower mesosphere does not show much seasonal or geographical variability [e.g., Connor *et al.*, 1994; Ricard *et al.*, 1996]. This correction only slightly increases our nighttime cooling rates, since the cooling rate due to $9.6 \mu\text{m}$ ozone emission is $<1 \text{ K day}^{-1}$ above 0.1 hPa [López-Puertas and Taylor, 2001]. For the eclipse simulations, this correction was not applied within umbral shadow regions.

[18] In all the runs reported here, CO_2 was set to a global constant value of 350 ppmv.

3.1.1.2. Simplified Model

[19] Since CLIRAD is rigorously validated up to 0.01 hPa only, we typically run NOGAPS-ALPHA with the model top at 0.005 hPa, with model layers at 0.01–0.005 hPa a heavily damped sponge region. In the simulations to be described, however, we extend the model to 0.0005 hPa in an effort to study possible far-field radiation of eclipse-generated gravity waves to higher altitudes.

[20] The dashed curve in Figure 3c shows a CLIRAD shortwave heating rate calculated off-line at a specific location in the eclipse path based on +8 hour temperature and constituent profiles from a NOGAPS-ALPHA control run, to be described later. At altitudes just above 0.1 hPa, the reduction with height of the ozone heating rates abates, and a secondary layer of radiative heating develops. That heating layer extends to the highest model altitudes.

[21] This secondary heating rate layer is problematic for two reasons. First, it extends to altitudes above 0.01 hPa (gray curve in Figure 3c) where CLIRAD is not validated and hence the heating rates are unreliable. Second, our primary focus is on eclipse-induced waves generated by reduced shortwave ozone heating in the stratosphere. This secondary high-altitude layer of radiative heating can produce additional thermal eclipse forcing that can potentially complicate or even mask the wave signals radiating upward from the reduced ozone heating in the stratosphere.

[22] To eliminate this secondary heating rate layer in this study, above 0.1 hPa we scaled down the ozone mixing

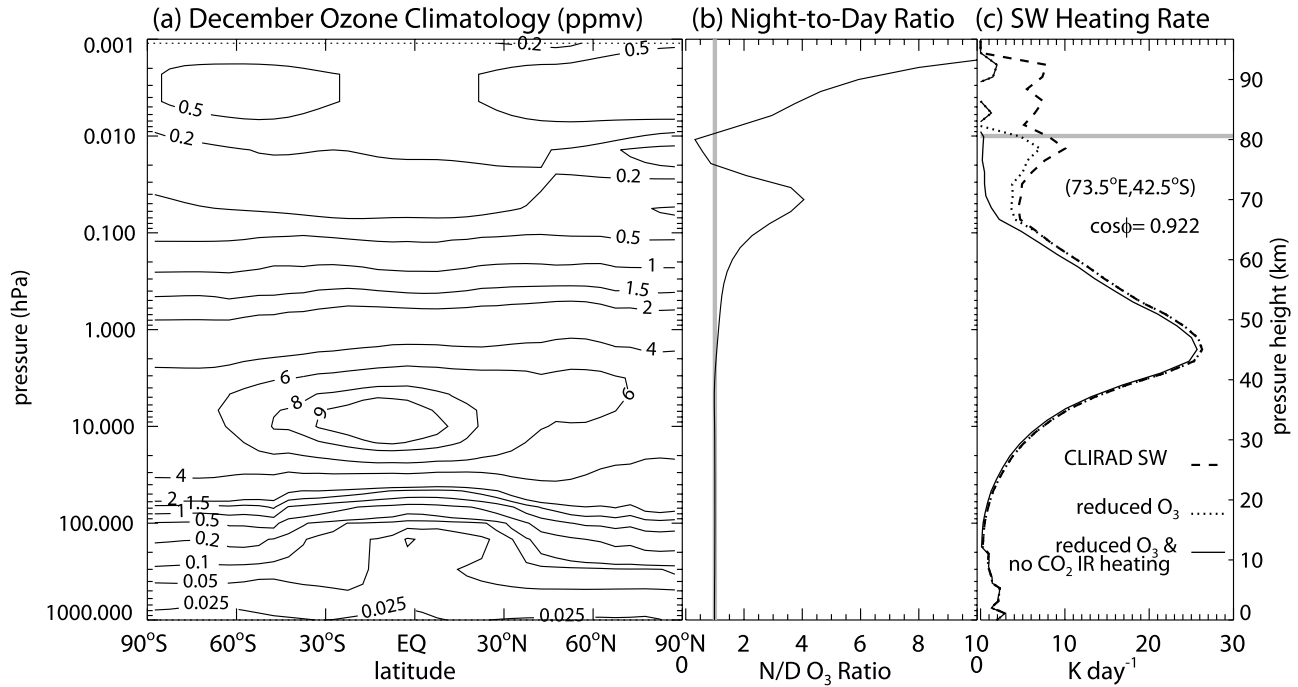


Figure 3. (a) Zonal-mean ozone mixing ratios (ppmv) for December used for NOGAPS-ALPHA daytime heating and cooling rate calculations. (b) Ozone night-to-day ratio, used to scale nighttime ozone mixing ratios in the cooling rate calculations. (c) CLIRAD radiative heating rates at indicated location from single column model (dashed curve). Remaining curves show changes after scaling down of high-altitude ozone in Figure 3a using equation (1) (dotted curve) and then further removal of infrared CO₂ heating rates (solid curve). Gray line shows nominal 0.01 hPa level, below which CLIRAD rates are valid.

ratios in Figure 3a using a pressure-dependent multiplicative coefficient

$$\epsilon(p) = \left(\frac{\log p - \log 0.01}{\log 0.001 - \log 0.01} \right)^2, \quad (1)$$

where p is model pressure in hPa, and $\epsilon(p) = 0$ for $p < 0.001$ hPa. The dotted curve shows the heating rate after imposing this ozone reduction. We see it eliminates nearly all the radiative heating at $p < 0.01$ hPa.

[23] From 0.1 to 0.01 hPa a residual contribution to the secondary heating rate layer remains, due mostly to CO₂ absorption in the near infrared. The solid curve shows the heating rate profile after CO₂ heating has been deactivated in CLIRAD. While the stratospheric heating is reduced slightly, the secondary layer is now almost completely eliminated.

[24] In what follows, we show results from NOGAPS-ALPHA runs in which we have eliminated CO₂ heating and reduced the high-altitude O₃ heating in this way, so that we can focus on atmospheric responses to reduced stratospheric shortwave heating due to the eclipse.

3.1.2. Hindcast Runs

[25] Our hindcast experiments use a T79L68 model formulation extending to 0.0005 hPa. A “cold start” initialization procedure is used in which analyzed winds, geopotential heights and moisture are read in at reference pressure levels on a $1^\circ \times 1^\circ$ grid and interpolated to the model’s quadratic Gaussian grid and hybrid σ – p levels.

Initial virtual temperatures are computed hydrostatically from the geopotentials. The model was then forwarded in time without assimilation update cycles using a model time step of 300 s.

[26] From 1000 to 10 hPa, these initialization fields were specified by archived NOGAPS analysis for 4 December 2002 at 0000 UTC, generated operationally at the Fleet Numerical Meteorology and Oceanography Center (FNMOC) by the then-operational Navy multivariate optimum interpolation (MVOI) system [Barker, 1992]. From 10 to 0.4 hPa we use FNMOC’s “STRATOI” analysis of winds and geopotentials [see Goerrs and Phoebus, 1992, section 4]. At altitudes above 0.4 hPa, where there are no Navy analysis fields for this date, we extrapolate the 0.4 hPa STRATOI fields upward by progressively relaxing them with increasing altitude to zonal-mean climatological winds from the UARS Reference Atmosphere Project [Swinbank and Ortlund, 2003] and temperatures from the 1986 COSPAR International Reference Atmosphere [Fleming et al., 1990]: for algorithm details, see Eckermann et al. [2004]. This final global initial state within NOGAPS-ALPHA is adjusted for hydrostatic balance, then run through a nonlinear normal mode initialization procedure [Errico et al., 1988] to improve dynamical balance and suppress spurious gravity wave generation due to unbalanced initial conditions.

[27] At the surface, ice concentrations, land/sea surface temperatures (SSTs) and snow depths are initialized using FNMOC analysis. Ice and SSTs are updated from archived

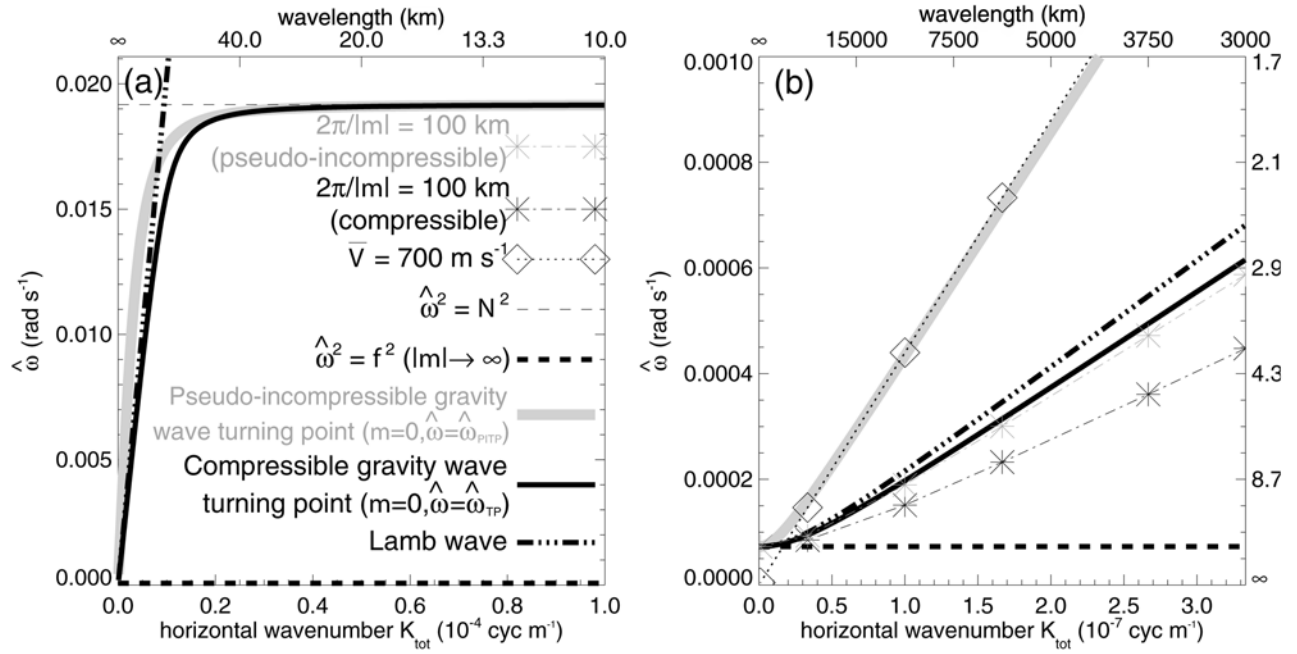


Figure 4. (a) Dispersion curves for Lamb waves (thick dot-dashed) and gravity waves at their turning points ($m = 0$) using fully compressible (black solid curve) and pseudo-incompressible (gray solid curve) dispersion relations, plotted versus horizontal wavenumber K_{tot} and intrinsic frequency $\hat{\omega}$. Horizontal dashed lines show the $\hat{\omega} = |f|$ and $\hat{\omega} = N$ limits. (b) Expansion of lower left corner of Figure 4a, showing space-time characteristic of eclipse shadow motion for $\bar{V} = 700 \text{ m s}^{-1}$ (dotted curve with diamonds) and dispersion curves for internal gravity waves of $2\pi/|m| = 100 \text{ km}$ (dot-dashed curves with asterisks) under both fully compressible (black) and pseudo-incompressible (gray) dispersion relations.

analysis every 24 hours: grid point values at the intervening times are linearly interpolated.

3.1.3. Eclipse Simulations

[28] The hindcast run described above for 4 December 2002 represents our control simulation. Our eclipse simulation repeats the same run, keeping everything the same until 0451 UTC when the eclipse begins. Then, at each model time step, the global $E_{UV}(\lambda, \phi, t)$ field at the current universal time t of the model simulation is read in, where (λ, ϕ) are longitude and latitude. These fields scale down the solar constant used in the radiative heating rate calculations, as

$$S(\lambda, \phi, t) = S_0[1 - E_{UV}(\lambda, \phi, t)]. \quad (2)$$

When eclipsing abates at 1011 UTC, the simulation proceeds as before with $E_{UV}(\lambda, \phi, t) = 0$.

[29] By simply projecting $E_{UV}(\lambda, \phi, t)$ in a vertical column through the atmosphere via equation (2), we ignore vertical variations in the UV obscuration pattern. These changes with height will be largest where the Sun is low in the sky ($\cos \phi \rightarrow 0$). Since E_{UV} values in Figure 1 are generally small near the terminator, omission of these effects here should not introduce significant errors given other uncertainties in our estimated $E_{UV}(\lambda, \phi, t)$ fields (see Appendix A).

[30] In common with other atmospheric models, NOGAPS-ALPHA usually updates its radiative heating and cooling rates every 1–2 hours. To simulate the radiative response of the atmosphere to rapidly moving eclipse

shadows via equation (2), we updated the radiative heating and cooling rates at every model time step, both in the control and eclipse simulations.

[31] In both runs, instantaneous global model fields were saved spectrally at one hour intervals.

3.1.4. Sensitivity to Anticipated Dynamical Responses

[32] Figure 4a plots horizontal wavenumber K_{tot} versus intrinsic frequency $\hat{\omega}$ within the nominal internal gravity wave ranges of $2\pi/K_{tot} \gtrsim 10 \text{ km}$ and $f^2 \lesssim \hat{\omega}^2 \lesssim N^2$, where f is the inertial frequency and N is the buoyancy frequency. The thick solid curve shows the fully compressible non-hydrostatic turning point curve, where vertical wavenumber $m = 0$ ($\hat{\omega} = \hat{\omega}_{TP}$) and the gravity wave reflects vertically. Lamb waves occur along the dot-dashed curve, which also approximately demarks the gravity wave turning point in the hydrostatic limit [see Marks and Eckermann, 1995, Figure 1]. These two curves nearly overlay at small K_{tot} , then begin to diverge at $K_{tot} \gtrsim 1\text{--}2 \times 10^{-5} \text{ cyc m}^{-1}$ (wavelengths $\lesssim 50 \text{ km}$), demarking the point at zonal wave numbers ~ 400 where hydrostatic dynamical cores such as NOGAPS-ALPHA start exhibiting errors due to omitted nonhydrostatic effects [see, e.g., Kasahara and Qian, 2000, Figures 2 and 4]. The large-scale eclipse shadows in Figure 1 are expected to force gravity waves with horizontal wavelengths of thousands of kilometers [Chimonas, 1970; Fritts and Luo, 1993], placing them in the far bottom left corner of Figure 4a, well away from this large K_{tot} region where the hydrostatic approximation fails. This justifies our use of a

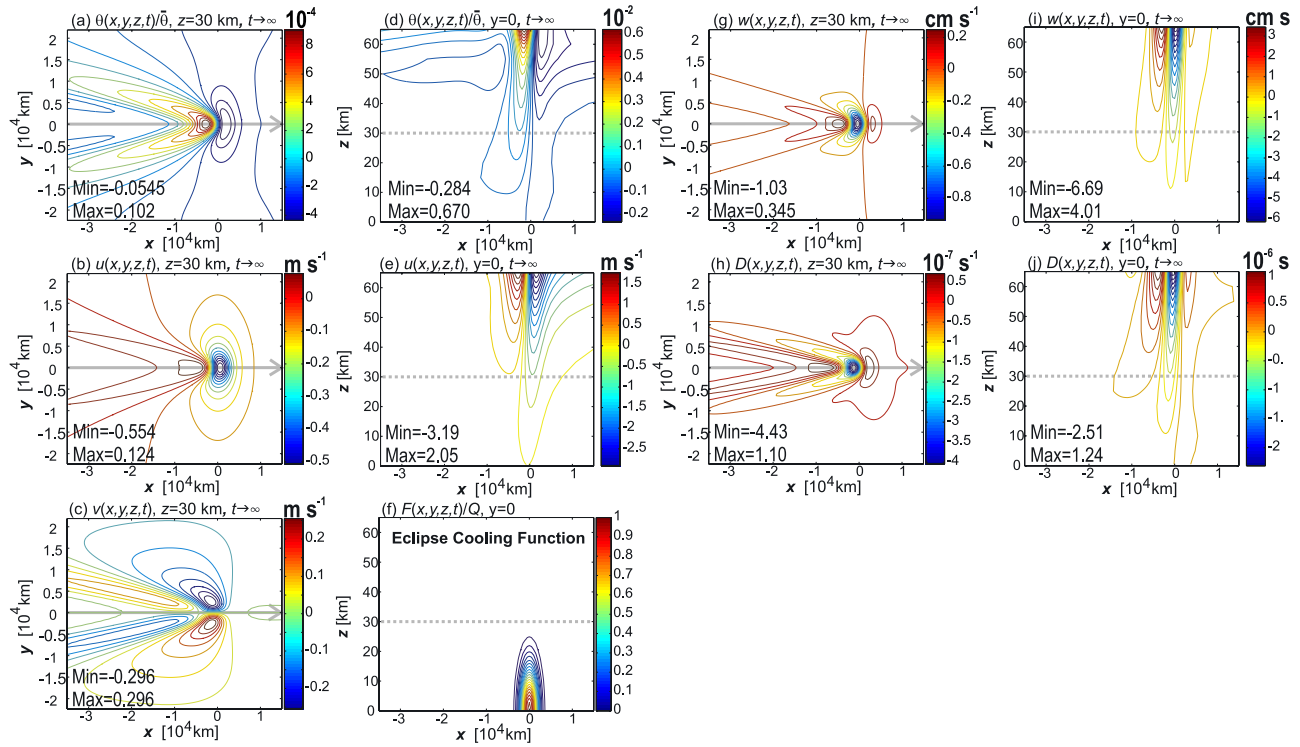


Figure 5. Fourier solutions of the gravity wave response to thermal eclipse forcing (8) based on the linearized pseudo-incompressible equations of *Fritts and Luo* [1993]. First column plots horizontal cross sections at $z = 30$ km above the peak in eclipse forcing F in (a) relative potential temperature, (b) zonal wind, and (c) meridional wind, with corresponding vertical cross section versus x along the eclipse shadow axis $y = 0$ (gray arrow) for (d) relative potential temperature and (e) zonal wind. (f) Vertical cross section of the eclipse heating rate perturbation F , normalized by its peak absolute value $Q = -12$ K day $^{-1}$, is plotted. Third column plots horizontal cross sections at $z = 30$ km above the peak F of (g) vertical velocity and (h) horizontal divergence, and fourth column plots vertical cross sections along $y = 0$ of (i) vertical velocity and (j) horizontal divergence.

T79 hydrostatic global spectral model to simulate eclipse-induced wave responses.

[33] Figure 4b focuses on this lower left portion of Figure 4a. Free-propagating (internal) gravity waves exist in the region below the solid black turning point curve ($\hat{\omega} < \hat{\omega}_{TP}$) and above the dashed curve ($\hat{\omega} > |f|$). The dotted line with diamonds shows intrinsic frequencies for a wave disturbance whose horizontal wavenumber is coaligned with an eclipse shadow velocity $\bar{V} = 700$ m s $^{-1}$ and whose horizontal phase speed is stationary in an “eclipse frame” moving at this speed \bar{V} : see section 3.2 for further details. This curve also represents the characteristic space-time scales of the thermal stratospheric forcing due to the eclipse. The wave field it generates is determined to first order by how directly these space-time forcing characteristics project onto various wave dispersion curves in Figure 4b [*Salby and Garcia*, 1987]. We see that this forcing curve lies above the compressible turning point and Lamb wave curves (since $\bar{V} > c_s \approx 320$ m s $^{-1}$, where c_s is the speed of sound), and so projects most directly onto a vertically evanescent (external) gravity wave response. The wave dispersion curves closest to the eclipse forcing curve are the (external) Lamb waves and high-frequency (long vertical wavelength) internal gravity waves, both of which have been

predicted by theoretical eclipse-forcing models [*Chimonas*, 1970, 1973; *Fritts and Luo*, 1993]. Vertically deep nonstationary gravity wave responses are also predicted by simple thermal forcing models where space-time scales of the source and gravity waves are mismatched, as here [e.g., *Holton et al.*, 2002].

[34] A global hydrostatic Eulerian spectral model such as NOGAPS-ALPHA can accurately simulate all of these anticipated wave responses [see, e.g., *Davies et al.*, 2003].

3.2. Fritts-Luo Gravity Wave Model

[35] To compare our NOGAPS-ALPHA results with existing models of eclipse-induced gravity waves, we consider the equations derived and solved by *Fritts and Luo* [1993]. They begin with the pseudo-incompressible equations of *Durran* [1989], which filter out acoustic and Lamb waves, then simplify further using the hydrostatic approximation, since nonhydrostatic wave responses are not anticipated (see Figure 4). Following *Chimonas* [1970], *Fritts and Luo* [1993] omit rotation, then derive linearized perturbation forms of the equations, seeking steady (stationary) wave solutions in a coordinate system (x, y, z) that moves in the x -direction at the eclipse shadow speed \bar{V} , which is assumed constant. Background winds are ignored, although

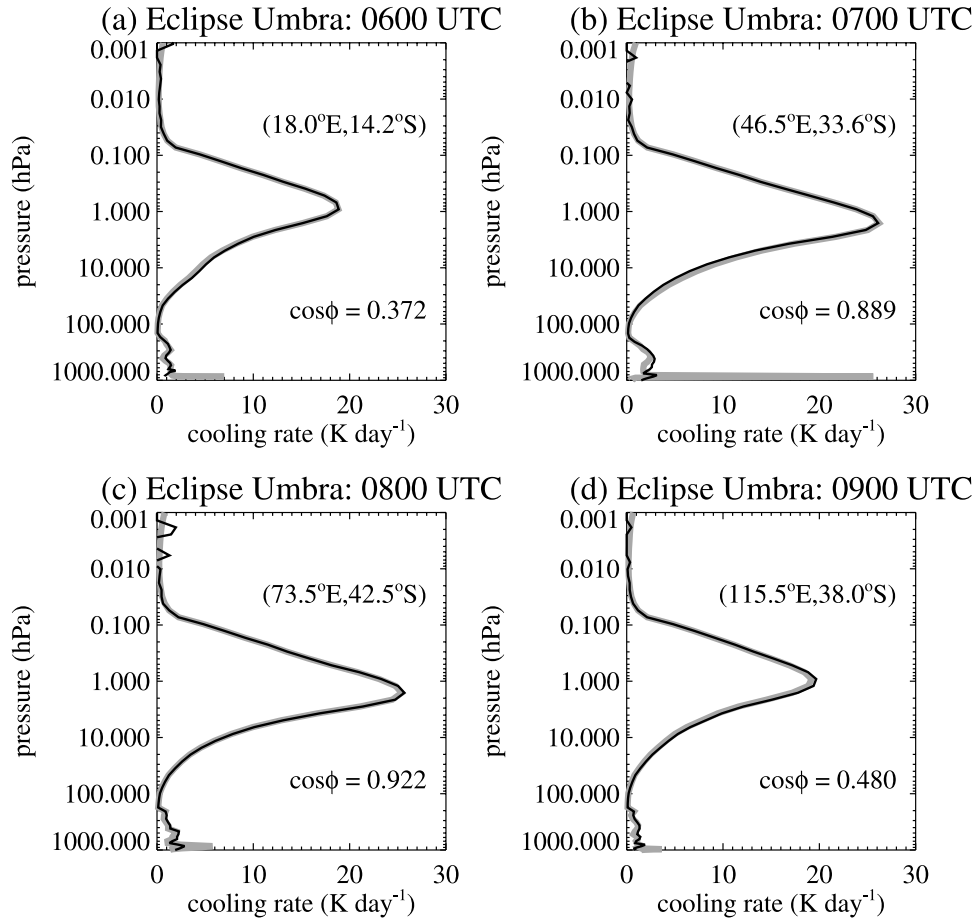


Figure 6. Gray curves show difference fields in total radiative heating rate between eclipse and control simulations, $Q'(p)$, at (a) 0600 UTC, (b) 0700 UTC, (c) 0800 UTC and (d) 0900 UTC, plotted here as (positive) cooling rates. Solid curves show corresponding $-Q_{eclipse}^{sw}(p)$ profiles, where $Q_{eclipse}^{sw}$ is the shortwave heating rate at the geographical location of totality in the absence of eclipse obscuration effects. These latter profiles were computed off-line with a single column model using profiles of temperature, water vapor, ozone, albedo and ground temperature from the NOGAPS-ALPHA control simulation at the indicated location and time. Differences lower down are due in part to cloud effects not included in the single column calculation.

a constant flow speed could be added to \bar{V} . The resulting equations are:

$$\bar{V}u_x + p_x/\bar{\rho} = 0, \quad (3)$$

$$\bar{V}v_x + p_y/\bar{\rho} = 0, \quad (4)$$

$$p_z/\bar{\rho} - g\theta/\bar{\theta} = 0, \quad (5)$$

$$u_x + v_y + w_z - wg/c_s^2 = F/\bar{\theta}, \quad (6)$$

$$\bar{V}\theta_x + \bar{\theta}N^2w/g = F, \quad (7)$$

where u , v , w , p and θ are, respectively, the perturbations of the velocity components, pressure, and potential temperature. The mean quantities $\bar{\theta}$ and $\bar{\rho}$ (atmospheric density)

are functions of z only. The speed of sound is c_s , the gravitational acceleration is g , and the mean buoyancy frequency is $N = (g\bar{\theta}_z/\bar{\theta})^{1/2}$.

[36] For the eclipse-induced diabatic heating rate perturbation, F , Fritts and Luo [1993] chose a Gaussian of the form

$$F = Q \exp \left[-\frac{(x^2 + y^2)}{2\sigma_r^2} - \frac{z^2}{2\sigma_z^2} \right], \quad (8)$$

with $\sigma_r = 1460$ km, $\sigma_z = 10$ km, and $|Q| = 12$ K day⁻¹ (the sign convention for Q is discussed below). Other parameter values in the Fritts-Luo model are: $N = 0.02$ s⁻¹, $g = 9.8$ m s⁻², $\Gamma = 2.7 \times 10^{-2}$ km⁻¹, and a scale height of 7.8 km. Note too that $z = 0$ in this model occurs at the height of the peak eclipse-induced cooling rate $|Q|$, not at the surface.

[37] We compute numerical solutions in the $t \rightarrow \infty$ limit using a Fourier method outlined in Appendix B. The first and third columns of plots in Figure 5 show horizontal cross sections, at $z = 30$ km above the peak eclipse forcing, of

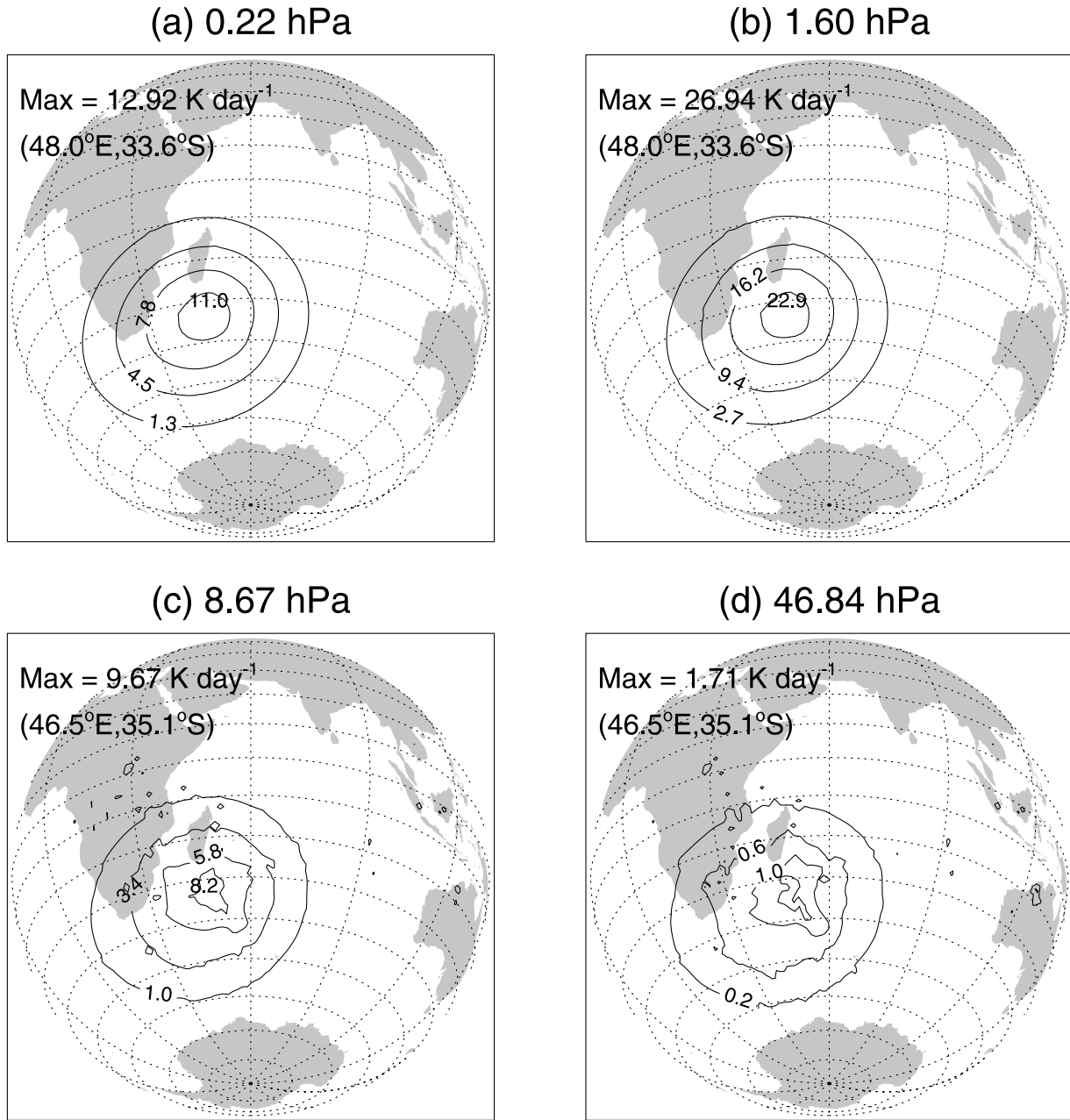


Figure 7. Maps of radiative cooling rates (K day^{-1}) due to the eclipse at 0700 UTC from NOGAPS-ALPHA runs, plotted at (a) 0.22 hPa, (b) 1.6 hPa, (c) 8.7 hPa, and (d) 46.8 hPa. Values and locations of maxima are given in the top left of each map.

wave-induced perturbations of relative potential temperature θ/θ , zonal wind u , meridional wind v , vertical velocity w and horizontal divergence $D = u_x + v_y$. The temperature and velocity plots can be compared to *Fritts and Luo* [1993, Figures 1 and 2], which span the much smaller horizontal subrange of $-1 \times 10^4 \text{ km} < x < 0$ and $-0.6 \times 10^4 \text{ km} < y < +0.6 \times 10^4 \text{ km}$. The Fourier solutions within this (x, y) subrange are similar in form and magnitude to those of *Fritts and Luo* [1993], apart from a uniform 180° phase difference. This sign ambiguity seems to originate in Q , which is set to 12 K day^{-1} by *Fritts and Luo* [1993]. However, F in (6) and (7) is a heating rate perturbation [Durrant, 1989], and so imposition of peak eclipse-induced

cooling via (8) implies $Q = -12 \text{ K day}^{-1}$, a sign convention we have used here.

[38] The second and fourth columns of plots in Figure 5 show corresponding vertical cross sections of the wave fields along the $y = 0$ eclipse shadow axis. The exception is Figure 5f, which profiles the normalized eclipse-induced cooling rate function F/Q , since the v field beside it is antisymmetric about $y = 0$ and thus its vertical cross section is featureless. These cross sections all show a vertically deep wave response (vertical wavelengths $\sim 100\text{--}200 \text{ km}$), which grows in amplitude with increasing altitude.

[39] Our Fourier solutions showed considerable sensitivity to our choice for Γ . The solutions in Figure 5 were

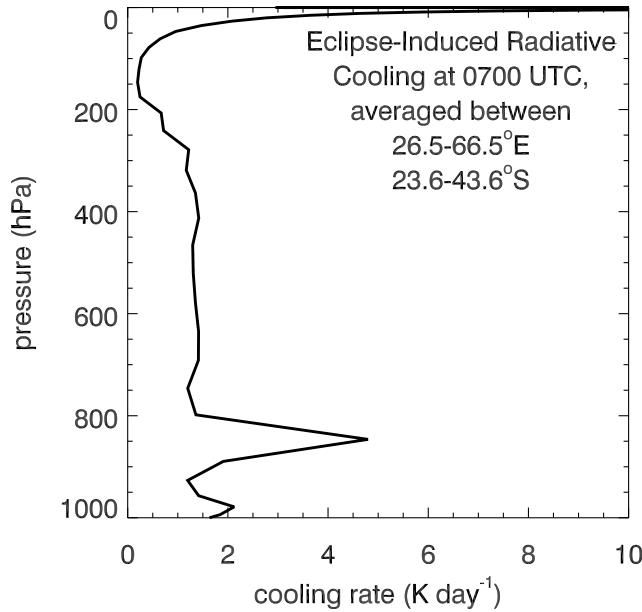


Figure 8. Eclipse-induced radiative cooling rates from NOGAPS-ALPHA runs at 0700 UTC, averaged over the indicated 40° longitude and 20° latitude band centered about the eclipse umbra location at this time.

derived using $\Gamma = 2.45 \times 10^{-2} \text{ km}^{-1}$, a value about 10% smaller than that used by *Fritts and Luo* [1993], which gave better agreement with their results. The reason for this sensitivity can be gleaned from Figure 4b, whose gray solid curve shows the gravity wave turning point curve under the pseudo-incompressible dispersion relation (B6) with rotation retained ($m = 0$, $\hat{\omega} = \hat{\omega}_{PTP}$). We see that the pseudo-incompressible turning point frequencies $\hat{\omega}_{PTP}$ exceed the fully compressible values $\hat{\omega}_{TP}$ (black solid curve), thus permitting a greater range of harmonic pairs (K_{tot} , $\hat{\omega}$) to be freely propagating gravity waves. Furthermore, the space-time characteristic curve of eclipse motion (dotted line with diamonds) essentially overlays this pseudo-incompressible turning point curve. Thus slight changes in \bar{V} or Γ which change the relative positions of these two curves allow for significant increases or decreases in forcing of freely propagating gravity wave harmonics in this model. More importantly, Figure 4b shows that the pseudo-incompressible solutions will overestimate internal gravity wave generation by the moving eclipse shadow, by allowing supersonic wave phase speeds to propagate vertically as internal gravity waves. This reflects a breakdown in the pseudo-incompressible approximation, which requires the Lagrangian timescales of these forced wave disturbances to be much longer than timescales for sound wave propagation [Durran, 1989], or equivalently, horizontal phase speeds to be much slower than c_s . As Figure 4b attests, this criterion is not satisfied generally for thermal forcing by supersonically moving eclipse shadows.

[40] Despite these caveats, these pseudo-incompressible *Fritts and Luo* [1993] solutions are valuable in providing guidance on the three-dimensional shapes and amplitudes of stationary gravity wave responses anticipated from broadly

realistic eclipse-induced thermal cooling of the stratosphere, for cross comparison with the NOGAPS-ALPHA results.

4. NOGAPS-ALPHA Results

4.1. Eclipse Radiative Cooling Rate Footprint

[41] In any given NOGAPS-ALPHA grid box, the net radiative heating rate profile $Q(p) = Q^{sw}(p) + Q^{lw}(p)$, where Q^{sw} is the shortwave solar heating, Q^{lw} is the longwave cooling contribution and p is model pressure. Gray curves in Figure 6 plot vertical profiles of $Q' = Q_{eclipse} - Q_{control}$, the difference in these net heating rate profiles between eclipse and control simulations, plotted at umbral shadow locations from 0600 UTC to 0900 UTC (see Figure 1a). These profiles all reveal uniformly negative heating rate perturbations Q' due to the eclipse UV obscuration E_{UV} and so are plotted in Figure 6 as (positive) cooling rates.

[42] Within these regions of totality, $E_{UV} = 1$ and thus from (2) shortwave heating is totally shut off ($Q^{sw}_{eclipse} = 0$). Thus, if the longwave cooling does not change significantly between eclipse and noneclipse conditions, then $Q' \approx -Q^{sw}_{control}$. To test this, the black curves in Figure 6 plot off-line estimates of $-Q^{sw}_{control}$ using saved output profiles from the control simulation at these times and locations. These $-Q^{sw}_{control}$ profiles essentially overlay the stratospheric Q' profiles.

[43] The gray Q' profiles in Figure 6 occur within totally eclipsed atmospheric regions. In penumbral regions ($0 < E_{UV} < 1$), reduced (rather than zero) solar shortwave heating occurs during eclipse passages, and so the radiative cooling rate signature of the eclipse is reduced here. To define the overall horizontal structure of these eclipse-induced cooling rate footprints, Figure 7 plots maps of Q' from the NOGAPS-ALPHA runs at 0700 UTC at 4 different pressure levels, ranging from the lower mesosphere (0.22 hPa) to the lower stratosphere (47 hPa). The horizontal structures generally resemble that of the corresponding 0700 UTC E_{UV} footprint in Figure 1f.

[44] Maps of tropospheric radiative heating rate perturbations like those in Figure 7 (not shown) reveal much greater spatial inhomogeneity, apparently related to cloud fields simulated in the model. To assess the potential for a net large-scale forcing effect [e.g., *Chimonas*, 1973], Figure 8 plots a mean 0700 UTC $Q'(p)$ profile averaged over a broad geographical region centered about the umbra. It reveals smaller but significant eclipse-induced radiative cooling rates throughout the troposphere, with forcing peaking in this case near 850 hPa.

4.2. Middle Atmospheric Responses

[45] We focus initially on the atmospheric responses at 0800 UTC, since they are morphologically similar (but of larger amplitude and size) to those simulated at earlier eclipse times. By 0800 UTC the eclipse shadow is moving near its limiting speed of $\sim 700 \text{ m s}^{-1}$ over oceanic regions where the Sun is high in the sky (Figures 1h and 2). Figure 9 plots maps of difference fields between eclipse and control runs at 1.6 hPa, a level near the peak in the eclipse-induced radiative cooling rate, and at 0.01 hPa, a region ~ 30 – 40 km above the peak eclipse cooling in a region where no local thermal forcing due to the eclipse is anticipated in these runs (see Figure 6).

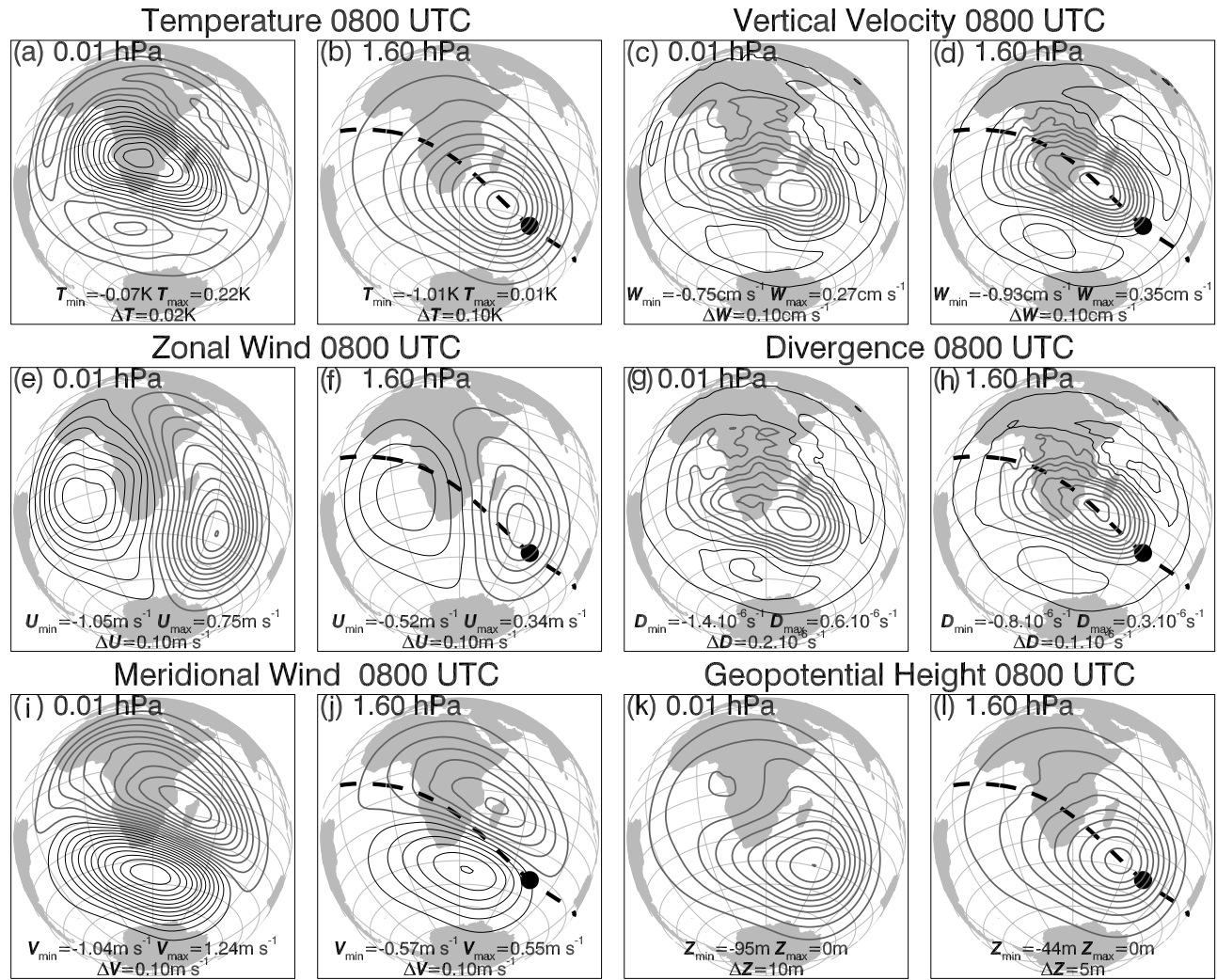


Figure 9. Polar orthographic maps of modeled atmospheric responses to eclipse passage at 0800 UTC at 0.01 hPa (columns 1 and 3) and 1.6 hPa (columns 2 and 4). Parameters plotted are (a–d) temperature T' and vertical velocity W' , (e–h) zonal wind U' and horizontal divergence D' , and (i–l) meridional wind V' and geopotential height Z' . The minimum and maximum values, contour interval and units are given at the bottom of each map. Positive values have black contours, and negative values have thicker gray contours. Dashed line shows passage of umbral shadow, extrapolated to longitudes west of Africa. Solid black circle shows 0800 UTC location of the umbra. 15×7 point longitude-latitude smoothing was applied to these fields.

[46] The horizontal structures of the temperature responses, $T' = T_{\text{eclipse}} - T_{\text{control}}$, differ notably at each altitude. At 1.6 hPa the response is mostly a uniform decrease that peaks at $T' = -1.0$ K slightly behind the umbral shadow. This reflects the direct atmospheric cooling effect of reduced shortwave ozone heating of this model layer due to obscuration of the solar disc. The integrated effect of this atmospheric temperature decrease is also seen in the geopotential heights, Z' , which show a similar structure to the 1.6 hPa T' field.

[47] The “far field” temperature response at 0.01 hPa is completely different. It is characterized by a warm central core, peaking at 0.22 K over Africa, surrounded by a belt of weaker negative T' values. Similar annular responses are simulated at both altitudes in vertical velocities, W' , and horizontal divergences, D' .

[48] The core of negative D' and W' values surrounded by a belt of weaker positive values implies a convergent circulation in which air moves inward toward a central point located near southern Africa, then descends, with weaker divergence and ascent at the outer edges. This is reflected in a zonal velocity response U' that is roughly zonally antisymmetric about the 20°E meridian near Africa: eastward of this meridian, a lobe of negative U' values occurs, peaking near the umbral shadow, while to the west of this meridian a lobe of positive U' values occurs well away from the moving eclipse shadow. Similarly, the meridional velocity response V' is approximately antisymmetric about a latitude circle: poleward, a lobe of positive V' values occurs, and equatorward, a lobe of negative V' values occurs. The peak magnitudes of all four horizontal velocity

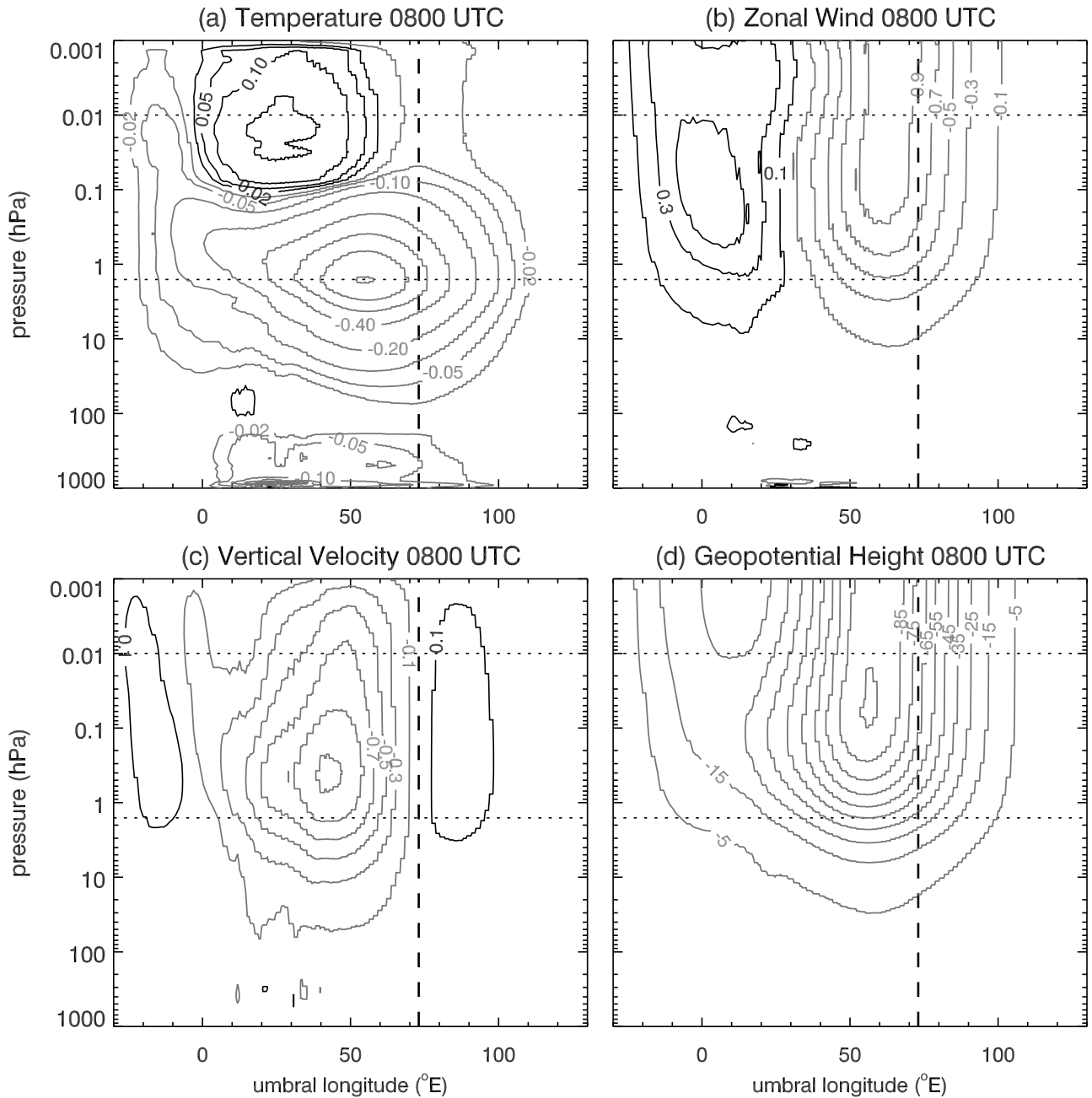


Figure 10. Vertical cross sections of 0800 UTC modeled atmospheric responses to eclipse passage along umbral trajectory (dashed curve in 1.6 hPa plots of Figure 9): (a) temperatures, contour interval 0.2 K, with ± 0.02 K, ± 0.05 K and ± 0.1 K contours also shown; (b) zonal wind, contour interval 0.2 m s^{-1} ; (c) vertical velocity, contour interval 0.2 cm s^{-1} ; and (d) geopotential height, contour interval 10 m. In all plots, positive values have black contours, and negative values have thicker gray contours. Horizontal dotted lines mark 0.01 hPa and 1.6 hPa levels mapped in Figure 9. Vertical dashed line shows 0800 UTC umbral shadow location.

lobes are about the same, roughly 0.5 m s^{-1} at 1.6 hPa and 1 m s^{-1} at 0.01 hPa.

[49] To study the vertical structure of these responses, Figure 10 plots altitude cross sections along the extrapolated umbral path depicted by the dashed curves in the 1.6 hPa plots of Figure 9. Temperature cross sections show a broad region of cold upper stratospheric anomalies due to eclipse-induced radiative cooling of this region (Figure 6). At

altitudes above 0.1 hPa, the response transitions to a weak warming in the wake of the eclipse shadow, giving way to a weaker cooling response near the Greenwich meridian that tilts westward with height. On descending through the stratosphere, the mean cooling response progressively weakens and disappears, giving way to a weak warming peak near 70 hPa before reappearance of temperature

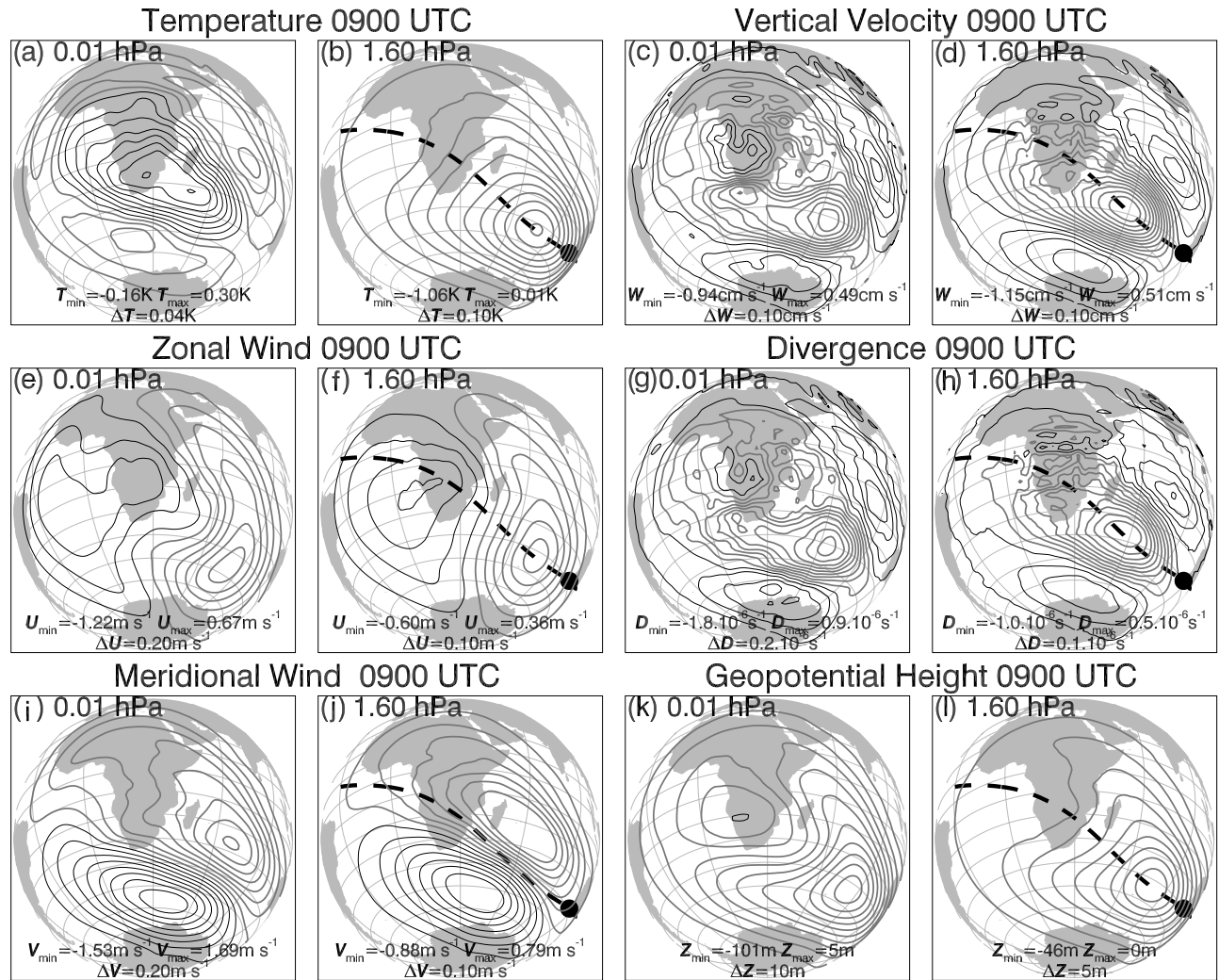


Figure 11. Same presentation as Figure 9 but plotting the modeled atmospheric response to the eclipse at 0900 UTC.

decreases in the troposphere due to direct radiative cooling of these layers (Figure 8).

[50] The two-lobed zonal wind response in Figure 10 is vertically very deep. The positive ($U' > 0$) lobe tilts noticeably to the west. The negative lobe tilts slightly eastward with height, though the U' responses at and ahead of the umbral shadow (vertical dashed curve) are almost columnar ($U'_z = 0$), as are the structures in vertical velocities and geopotential heights at these locations. Apart from the increase in overall size and amplitude, the most notable change in 0800 UTC fields compared to earlier times is greater eastward tilting with height of the middle-atmospheric responses. For example, the vertical cross sections of Z' in Figure 10d reveal greater eastward tilting with height of the response behind the umbral shadow, associated with formation of an isolated Z' minimum at high altitudes just east of the Greenwich meridian. The horizontal 0.01 hPa Z' map in Figure 9k shows this is due to formation of a weak V-shaped response.

[51] By 0900 UTC, bow-wave-like responses become much stronger. For example, Figure 11 reveals Z' responses

at both altitudes with much clearer V-shaped structure, and formation of weak positive anomalies over Africa at 0.01 hPa. At that same location and altitude, positive W' and D' anomalies also arise. These bow-wave responses distort the previously symmetric zonal winds responses U' , particularly at higher altitudes (Figure 11f). Associated with this is greater eastward tilting of the vertical cross sections of U' , W' and Z' in Figure 12. The direct thermal cooling signatures of the eclipse in the stratosphere and troposphere in Figure 12a are now separated by a distinct region of weak positive temperature anomalies in the lower stratosphere and mesosphere behind the eclipse shadow, indicating both upward and downward propagation of bow-wave-like responses from upper stratospheric thermal eclipse forcing.

[52] Small-scale horizontal structure is seen in W' in Figure 12c over the African longitudes. This seems to originate from changes in the tropospheric shortwave cloud forcing over the African land mass, which modifies the convective clouds and the properties of explicitly resolved convectively generated short-wavelength gravity waves, which propagate to high altitudes. Their effects are evidenced

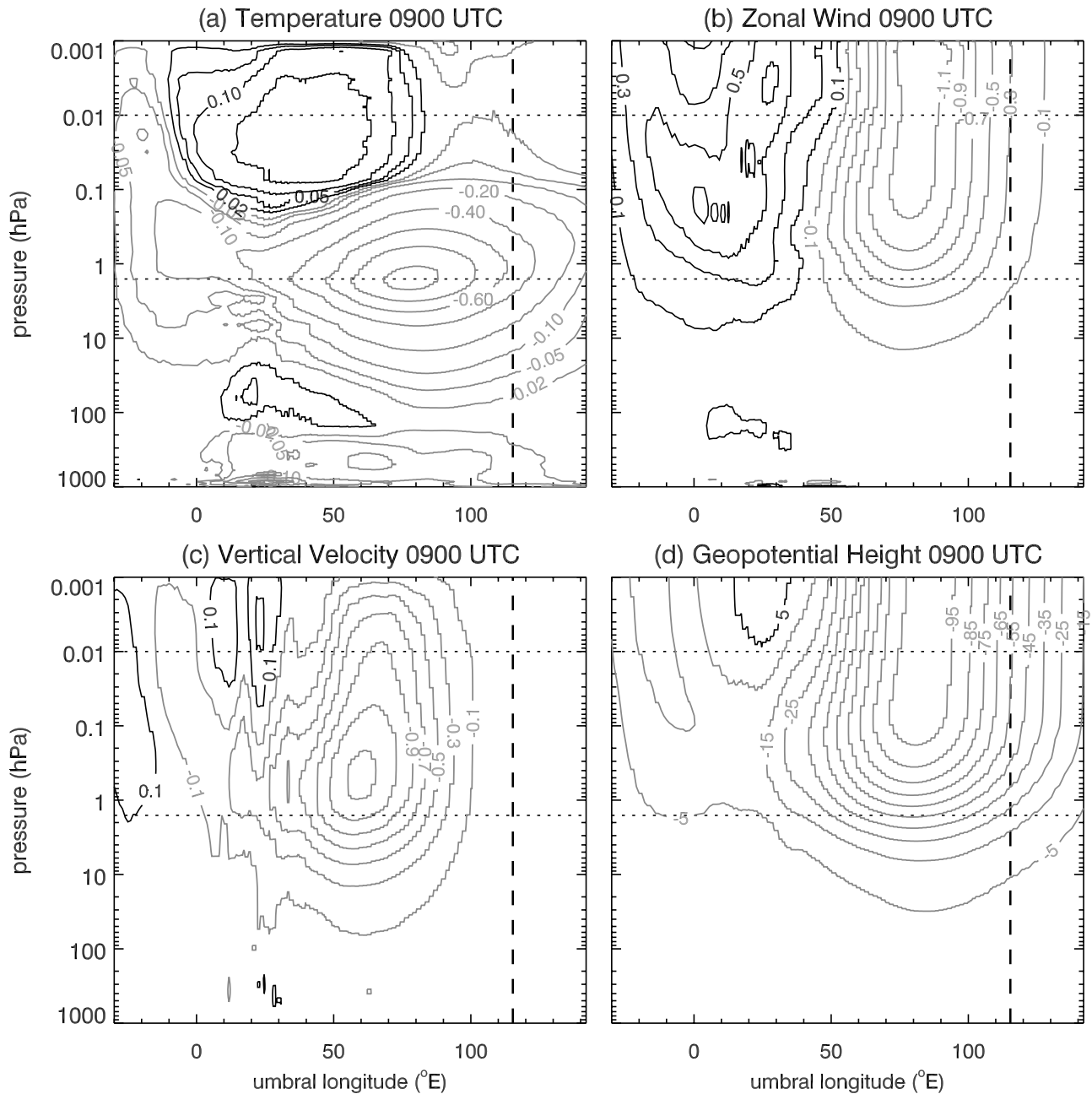


Figure 12. Same presentation as Figure 10 for the 0900 UTC modeled atmospheric response to eclipse passage: (a) temperatures, contour interval 0.2 K, with ± 0.02 K, ± 0.05 K and ± 0.1 K contours also shown; (b) zonal wind, contour interval 0.2 m s^{-1} ; (c) vertical velocity, contour interval 0.2 cm s^{-1} ; and (d) geopotential height, contour interval 10 m. Vertical dashed line shows 0900 UTC umbral shadow location.

by the noisier nature of the W' and D' fields in Figure 11, even after significant horizontal smoothing.

[53] As the eclipse nears its end by 1000 UTC (Figure 11), Figure 13 reveals bow wave-like responses dominating at high altitudes. For example, the symmetric two-lobe zonal wind response at earlier times has been largely replaced in Figure 13b by a well-defined V-shaped pattern that is approximately symmetric about the umbral shadow path (dotted green line). Similar V-shaped responses are also seen in temperature, vertical velocity and geopotential height in Figures 13a, 13c, and 13d.

4.3. Tropospheric Responses

[54] Figure 12a reveals midtropospheric cooling of $\sim 0.1 \text{ K}$ due to local radiative cooling within the eclipse shadow (Figure 8). Near the surface, however, much larger atmospheric temperature drops have been measured over land during eclipses due to radiative surface cooling and accompanying changes in turbulent fluxes of latent and sensible heat [e.g., *Segal et al.*, 1996]. To investigate this in NOGAPS-ALPHA, Figure 14 plots the air temperature response T'_S at 0700 UTC in the lowest full model layer,

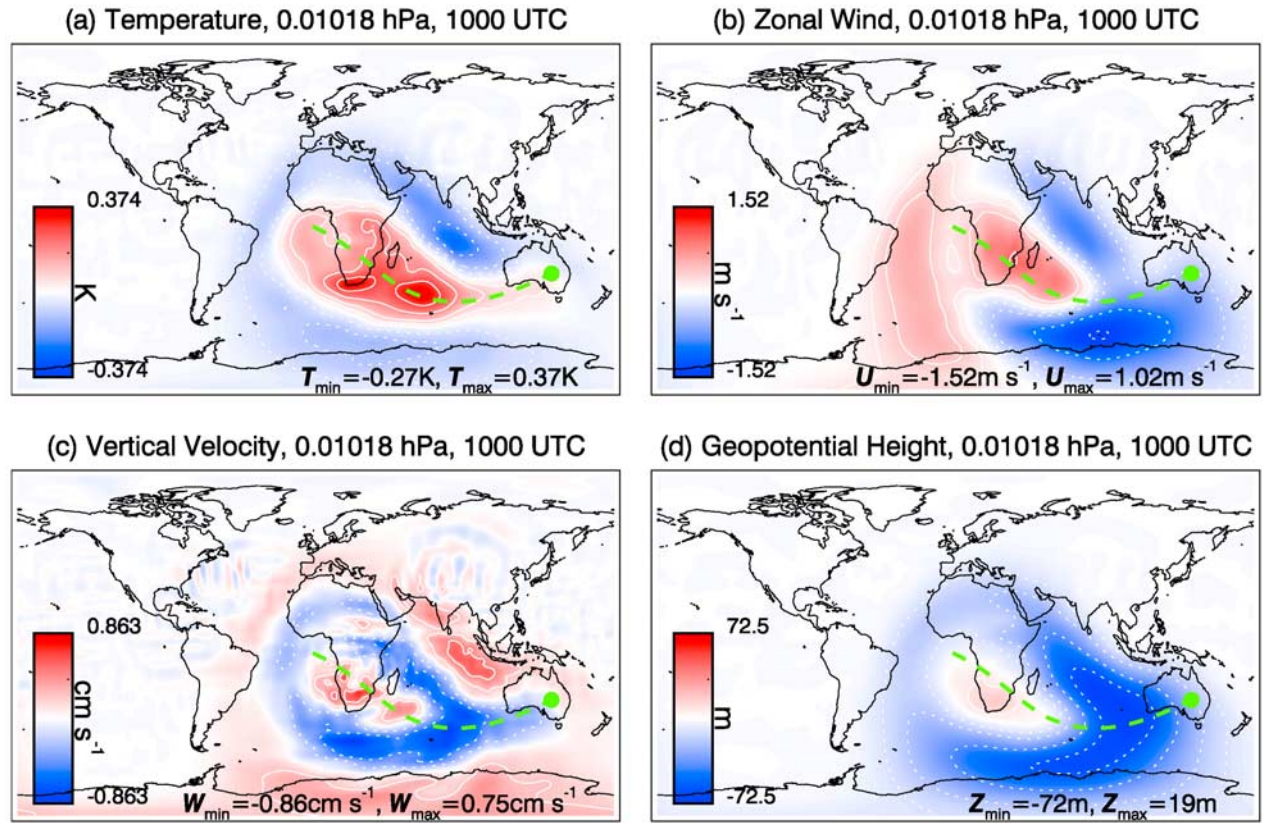


Figure 13. Maps of modeled atmospheric responses to eclipse at 1000 UTC at 0.01 hPa in (a) temperature, (b) zonal wind, (c) vertical velocity, and (d) geopotential height. Scales and units are given in the color bar, and minimum and maximum values at the bottom of each plot. Positive (negative) values have white solid (dotted) contours. These contours are every 0.1 K with ± 0.05 K contours also shown (Figure 13a), ± 0.2 m s⁻¹, ± 0.4 m s⁻¹, ± 1 m s⁻¹ and ± 1.5 m s⁻¹ (Figure 13b), ± 0.25 cm s⁻¹ and ± 0.5 cm s⁻¹ (Figure 13c), and every 20 m with ± 10 m contours also shown (Figure 13d). Thick dashed line shows passage of umbral shadow, and solid circle shows its final location just after 0900 UTC (see Figure 1). 15×7 point longitude-latitude smoothing was applied to these fields.

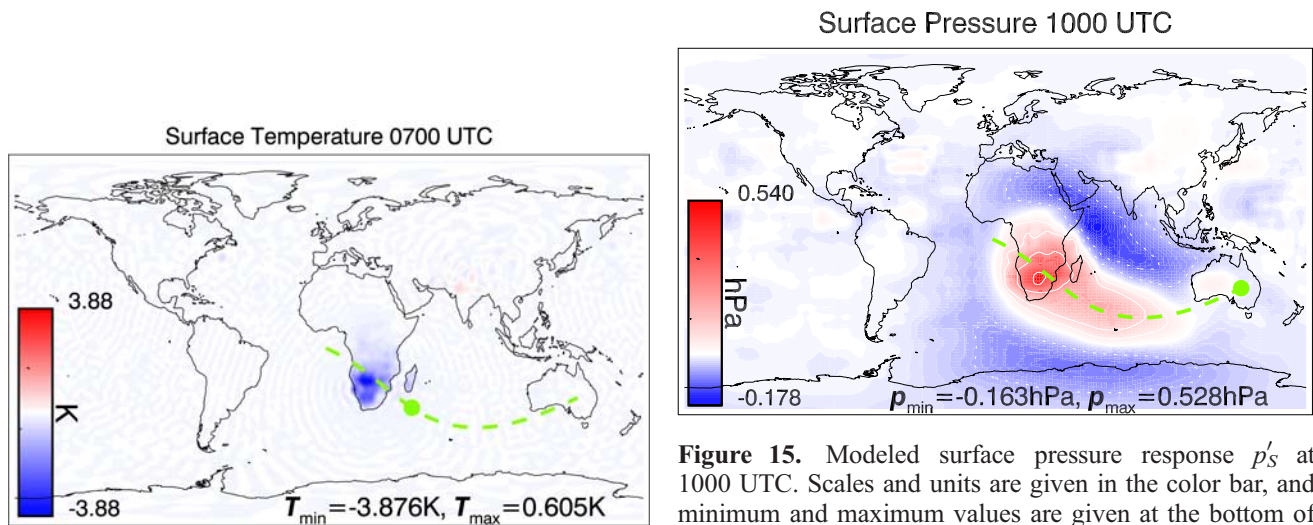


Figure 14. Modeled surface air temperature response T'_S at 0700 UTC. Scales and units are given in the color bar, and minimum and maximum values are given at the bottom of the map. Thick dashed line shows passage of umbral shadow, and solid circle shows its current location.

Figure 15. Modeled surface pressure response p'_S at 1000 UTC. Scales and units are given in the color bar, and minimum and maximum values are given at the bottom of the map. Positive (negative) values have white solid (dotted) contours: values are ± 0.05 hPa, ± 0.1 hPa, 0.3 hPa and 0.5 hPa. Thick dashed line shows passage of umbral shadow, and solid circle shows its final location just after 0900 UTC (see Figure 1). 15×7 point longitude-latitude smoothing was applied to these fields.

Table 1. Differences Between *Fritts and Luo* [1993] and NOGAPS-ALPHA Wave Solutions in Response to Thermal Stratospheric Eclipse Forcing

Parameter	<i>Fritts and Luo</i> [1993]	NOGAPS-ALPHA
<i>Major Differences</i>		
Dispersion relation	pseudo-incompressible	compressible
Shadow speed \bar{V}	constant	time-varying ^a
Eclipse cooling	constant ^b	variable ^c
Peak cooling	12 K day ⁻¹	~27 K day ⁻¹
Gravity wave solutions	stationary in \bar{V} frame	no restriction
Lamb waves	no	yes
Times	$t \rightarrow \infty$ limit	hourly
<i>Minor Differences</i>		
Wind/shear	no	yes
Geometry	Cartesian	spherical
Rotation	no	yes

^aSee Figure 2.^bSee equation (8).^cSee Figures 1 and 6.

located just 13 m above the ground for surface pressures of ~1000 hPa. We see atmospheric cooling of up to ~4 K that is confined over land (southern Africa and Madagascar). These values are within the 2–10 K range reported in both near-surface measurements [e.g., *Anderson et al.*, 1972; *Segal et al.*, 1996; *Eaton et al.*, 1997] and mesoscale model simulations [*Gross and Hense*, 1999; *Vogel et al.*, 2001] during previous eclipse passages.

[55] Figure 15 plots the 1000 UTC surface pressure response p'_S . Unlike the corresponding T'_S map (not shown), p'_S exhibits a coherent large-scale response over both land and ocean that is very similar in overall form to the bow-wave structures encountered at high altitudes in Figure 13 at this time. Amplitudes here are ~0.1–0.5 hPa, having increased with time during the eclipse passage, with the peak values clustered over the southern African land mass.

5. Discussion

[56] We now compare our simulated atmospheric responses to this solar eclipse in NOGAPS-ALPHA with some relevant observations and theories.

5.1. Stratospheric Bow Wave Theory

[57] The primary goal of the NOGAPS-ALPHA runs was to see whether reduced stratospheric ozone heating during the eclipse generated a large-scale internal gravity wave at higher altitudes with the bow-wave form and amplitudes predicted by the linear models of *Chimonas* [1970] and *Fritts and Luo* [1993]. To facilitate this comparison, we regenerated the *Fritts and Luo* [1993] gravity wave solutions in Figure 5. Exact correspondences between these solutions and our NOGAPS-ALPHA results are not expected because of a number of differences between the two formulations, the more important of which are summarized in Table 1.

[58] For this particular eclipse, for example, the NOGAPS-ALPHA runs gave peak eclipse-induced radiative cooling rates of ~27 K day⁻¹: see, e.g., Figures 6c and 7b. The bow-wave model of *Fritts and Luo* [1993] adopted a constant peak cooling rate $|Q|$ of 12 K day⁻¹ (see section 3.2), while *Chimonas* [1970] used ~9 K day⁻¹ [see *Murgatroyd and*

Goody, 1958; *Davies*, 1982]. Thus our NOGAPS-ALPHA simulations for this one specific eclipse indicate that earlier model studies have underestimated the strength of this peak eclipse-induced stratospheric thermal forcing by a factor of 2–3.

[59] Atmospheric responses in NOGAPS-ALPHA appeared at high altitudes quickly and rapidly expanded both meridionally and zonally. This indicates additional forcing of gravity waves that are nonstationary with respect to eclipse motion and thus not captured by the *Fritts and Luo* [1993] model. These waves arise because of more realistic space-time variations in thermal eclipse forcing (e.g., variable \bar{V} and Q) in the NOGAPS-ALPHA runs [e.g., *Holton et al.*, 2002]. As a result, the simulated NOGAPS-ALPHA responses at early times showed near-columnar annular or symmetric responses (Figures 9 and 10) that differed from bow-wave predictions. However, by 1000 UTC these early-stage responses transitioned to new forms more reminiscent of bow-wave model predictions. This is consistent with the long time limit ($t \rightarrow \infty$) of the *Fritts and Luo* [1993] solutions: fully compressible vertical group velocity calculations based on wavelength-frequency pairs in Figure 4b indicate that even the very long vertical wavelength internal gravity wave modes can take several hours to propagate to altitudes 30–40 km above the stratospheric eclipse forcing.

[60] At these later times there are clear similarities between the 0.01 hPa NOGAPS-ALPHA responses and the *Fritts and Luo* [1993] solutions in Figure 5. For example, Figure 5c predicts an antisymmetric meridional wind response V' about the $y = 0$ axis of the eclipse shadow motion, distorted downstream by bow-wave effects, with negative (positive) perturbations to the north (south) and peak magnitudes of ~0.25 m s⁻¹ at 30 km above the eclipse forcing. The NOGAPS-ALPHA V' response at 0900 UTC (Figure 11i) has a similarly phased antisymmetric form about the umbral shadow trajectory, but has larger peak magnitudes of ~1.7 m s⁻¹. The *Fritts and Luo* [1993] zonal velocity response U' in Figure 5b is symmetric about $y = 0$, with a strong negative lobe ahead of the eclipse, and a weaker V-shaped positive lobe behind it. NOGAPS-ALPHA 1000 UTC fields in Figure 13b show a similar structure, though with less difference between the leading and lagging lobe amplitudes. The *Fritts and Luo* [1993] temperature response in Figure 5a is symmetric about $y = 0$, dominated by a warm anomaly in the wake of the eclipse, peaking at a relative amplitude of about 10⁻³: for a mean 0.01 hPa temperature of ~200 K, this yields $T' \sim 0.2$ K. Warm symmetric V-shaped anomalies in the wake of the eclipse are also seen in NOGAPS-ALPHA fields, with a peak magnitude of ~0.3–0.4 K (Figures 11a and 13a).

[61] The vertical velocity and divergence responses in Figures 5g and 5h, respectively, are predicted to have a symmetric three-lobe structure, with weak positive anomalies ahead of the eclipse, a strong V-shaped negative anomaly immediately behind the umbra and a third weaker V-shaped positive anomaly forming further behind the umbra (see also Figure 5j). These two symmetric lagging lobes are both reproduced in the NOGAPS-ALPHA W' and D' fields. For example, Figures 11c and 11g show this second positive lagging lobe having just formed over Africa within the main negative lagging lobe. Both positive and

negative anomalies become larger and more V-shaped by 1000 UTC (Figure 13c).

[62] The vertical cross sections of the *Fritts and Luo* [1993] solutions in Figure 5 all show vertically deep responses that tilt eastward with increasing height, consistent with long vertical wavelength gravity waves that are stationary in a frame moving eastward at speed \bar{V} . Deep eastward tilted responses are also seen in the 0900 UTC NOGAPS-ALPHA velocity and geopotential height cross sections in Figure 12. Similar structure is masked in the temperature cross sections in Figure 12a because of a larger mean temperature decrease in the upper stratosphere due to local radiative cooling.

[63] In summary, the mesospheric NOGAPS-ALPHA fields at 0900–1000 UTC show clear evidence of a large-scale V-shaped internal gravity wave forced by radiative cooling of the stratosphere within the eclipse shadow. The overall horizontal, vertical and amplitude structures agree broadly with the predictions of *Fritts and Luo* [1993]. In particular, our results confirm their findings that mesospheric wave amplitudes are weak, which may explain the difficulty in observing this wave response during eclipse passages.

5.2. Middle Atmospheric Observations

[64] Some rocket soundings of the middle atmosphere have reported temperature decreases in the 5–12 K range at 50–60 km altitude during eclipse passages [*Ballard et al.*, 1969; *Quiroz and Henry*, 1973; *Randhawa*, 1974; *Schmidlin and Olsen*, 1984]. *Quiroz and Henry* [1973] and *Schmidlin and Olsen* [1984] also reported substantial increases in meridional wind speeds, peaking at 20–40 m s⁻¹ at ~60 km, which *Quiroz and Henry* [1973] interpreted as a balanced circulation response to eclipse-induced changes in the lateral temperature gradients. Our NOGAPS-ALPHA simulations were unable to reproduce these observations. We found no evidence of wind or temperature responses anywhere near this large in our model fields at 50–60 km: temperature decreases here were ≤ 1 K, and horizontal wind changes were a few meters per second at most (see, e.g., Figure 12).

[65] Several points are worth noting. First, rocketsondes measure instantaneous profiles with small-scale gravity wave perturbations superimposed, and the typical r.m.s. amplitudes of these oscillations at 50–60 km are ~ 10 m s⁻¹ for horizontal winds and ~ 2 –5 K for temperature [*Eckermann et al.*, 1995]. Given wave periods as short as 5–10 min, serendipitous phasing among gravity waves in sequential rocket profiles during eclipse passages could yield wind and temperature changes of the order of those reported, but which would have no physical connection to the eclipse. Since this phasing argument should just as easily produce warming, it cannot explain why all the studies have observed strong cooling, although there are other observations that have reported no measurable changes in middle atmospheric winds or temperatures during eclipses [*Randhawa*, 1973; *Ball et al.*, 1980].

[66] More detailed observations would clearly help. For example, ground-based temperature and wind (Doppler) lidars with day-night capabilities [e.g., *Alpers et al.*, 2004] could acquire data with the necessary time-height resolution

to separate mean and gravity wave components at these altitudes during a solar eclipse.

5.3. Bow Wave Response in Surface Pressure

[67] The NOGAPS-ALPHA surface pressure response p'_S at 1000 UTC in Figure 15 exhibits a large-scale bow-wave-like structure very similar to that seen in the high-altitude responses in Figure 13. Stratospheric eclipse cooling should radiate gravity waves to both higher and lower altitudes [*Chimonas*, 1970]. For the March 1970 eclipse, *Chimonas and Hines* [1970] predicted such downward radiation of gravity waves should yield surface pressure oscillations $p'_S \sim \pm 0.01$ hPa. These values are an order of magnitude or more smaller than our simulated amplitudes in Figure 15, which are in the 0.1–0.5 hPa range. However, these amplitudes are within the ± 0.1 –1 hPa range observed in microbarograph data during eclipses [see, e.g., *Anderson et al.*, 1972; *Seykora et al.*, 1985; *Jones et al.*, 1992; *Aplin and Harrison*, 2003]. Thus our result is broadly consistent with observations, but seems to be inconsistent with standard stratospheric bow wave theory.

[68] The observations of *Anderson et al.* [1972] led *Chimonas* [1973] to the same conclusion. He proposed an alternative model for these observations in terms of V-shaped Lamb wave patterns forced in the troposphere. Lamb waves are vertically external modes that propagate laterally at the speed of sound. Lamb wave energies and pressure amplitudes decay with height above the surface, and can be efficiently forced by diabatic forcing near the surface [*Lindzen and Blake*, 1972].

[69] NOGAPS-ALPHA produced a strong surface air temperature decrease over land (Figure 14), which is also broadly consistent with previous eclipse observations and relatively well understood in terms of modified surface and turbulent heat transport [e.g., *Segal et al.*, 1996]. This temperature drop should also modify pressure, and indeed the largest pressure increases in Figure 15 are also observed over southern Africa. Similar pressure increases over land were simulated by *Prenosil* [2000] using a mesoscale model for the August 1999 solar eclipse over Europe. However, since the temperature responses in Figure 14 are confined to land rather than moving with the eclipse shadow, it is not clear whether this land-locked thermal forcing could generate the large-scale bow-like pressure disturbance in Figure 15.

[70] *Chimonas* [1973] proposed Lamb-wave forcing due to reduced shortwave heating of tropospheric cloud layers within eclipse shadows. Figure 8 reveals net reductions in radiative heating in the troposphere in the NOGAPS-ALPHA simulations that are coherent over and move with the eclipse shadow over both land and ocean. Thus they are a viable tropospheric forcing term for the large-scale surface pressure response in Figure 15.

6. Conclusions

[71] Our NOGAPS-ALPHA simulations reveal clear evidence of a three-dimensional bow wave response to eclipse-induced radiative cooling of the stratosphere, as originally predicted by *Chimonas* [1970] and *Fritts and Luo* [1993]. Within the eclipse shadow, NOGAPS-ALPHA simulates an induced radiative cooling rate in the stratosphere that peaks

at $\sim 27 \text{ K day}^{-1}$, a forcing 2–3 times larger than assumed in these earlier stratospheric bow wave models.

[72] The bow wave generated by this thermal stratospheric eclipse forcing appears most clearly in NOGAPS-ALPHA fields at mesospheric heights near the end of the eclipse at 0900–1000 UTC, a finding consistent with finite vertical propagation times of gravity wave modes from their upper stratospheric source. These eclipse-induced bow-wave fields have small amplitudes, yielding temperature changes $\lesssim 1 \text{ K}$ and horizontal wind changes $\lesssim 2\text{--}3 \text{ m s}^{-1}$. These findings support the small middle atmospheric responses predicted by *Fritts and Luo* [1993] but contradict the much larger responses inferred from rocketsonde measurements by *Quiroz and Henry* [1973] and *Schmidlin and Olsen* [1984].

[73] Atmospheric surface pressures in NOGAPS-ALPHA at 1000 UTC also show a clear three-dimensional bow-wave response of amplitude $\sim 0.1\text{--}0.5 \text{ hPa}$, values consistent with previous surface pressure measurements during eclipse passages. Surface air temperatures in NOGAPS-ALPHA show drops of up to 4 K during the eclipse over land, and net radiative cooling occurs throughout the troposphere within eclipse shadows. These or other diabatic changes to the troposphere likely provide the forcing for this wavelike surface pressure disturbance [e.g., *Chimonas*, 1973].

[74] Future work could seek to apply this global modeling strategy to other eclipse events to see if these findings are general or specific to this particular eclipse. A higher-altitude global model that incorporates realistic mesospheric and thermospheric radiative heating and cooling would yield more realistic simulated middle atmospheric responses to the eclipse. Additional high-resolution middle atmospheric observations during eclipse passages would also be useful in investigating the origin of ongoing large discrepancies between rocketsonde data and model predictions.

Appendix A: Specifying the Solar UV Eclipse Shadow of 4 December 2002

[75] The standard USNO eclipse metric is the eclipse magnitude (or phase), E_M , the fraction of the Sun's diameter occulted by the lunar shadow at any given geographical location. If the apparent diameters of the lunar and solar disks are D_L and $D_S = 2R_S$, respectively, and the separation between their centers is δ , then

$$E_M = \frac{(D_L + D_S)/2 - \delta}{D_S}. \quad (\text{A1})$$

[76] The maximum eclipse magnitude $(E_M)_{\max}$ occurs when $\delta = 0$ (concentric lunar and solar disks). For total eclipses, $(E_M)_{\max} \geq 1$ since $D_L \geq D_S$; for the 4 December 2002 total eclipse, $(E_M)_{\max} = 1.02437$ [*Espenak and Anderson*, 2001].

[77] *Espenak and Anderson* [2001, Figure 1] plots paths of constant E_M in intervals of 0.2, rather than just the limiting umbral ($E_M = 1$) and penumbral ($E_M = 0$) paths given in Figure 1a. Those data show that, within the shadow region, E_M varies approximately linearly with great circle distance from the central total eclipse region to the penumbral perimeter, and so we specify E_M in this way using

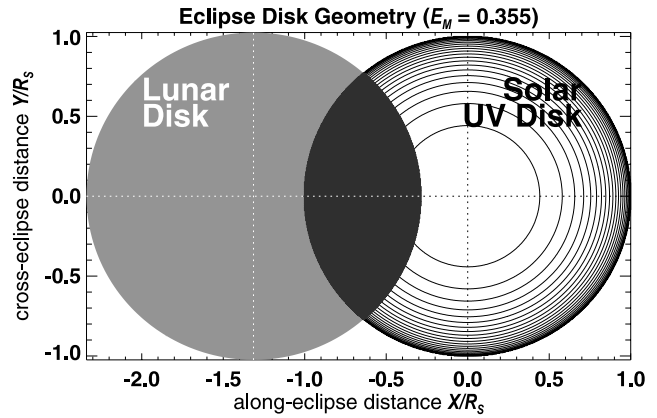


Figure A1. Geometry of the eclipse as a function of distances (X , Y) from the center of the solar disk, normalized by solar disk radius R_S , for $E_M = 0.355$ and $(E_M)_{\max} = 1.02437$. Lunar disk (shown in gray) moves along X axis and progressively obscures the solar disk. Obscured surface area A_{Ob} is shaded dark gray. Contours on solar disk show normalized UV limb darkening contours from equation (A11). Contour interval is 0.05 and maximum value is 0.975.

linear interpolation along great circle paths from the central umbral region to the penumbral perimeter.

[78] This interpolation procedure is straightforward when all parts of the eclipse shadow strike the surface of the Earth so that the penumbral perimeter is closed, as in Figure 1g. During the beginning and end phases of the eclipse, however, only a part of the two-dimensional penumbral disc (defining where the Moon obscures the Sun) actually strikes the Earth's surface, which causes the penumbral perimeter to be open as the partially eclipsed Sun disappears from view at the solar terminator (see, e.g., Figures 1b–1e and 1i–1l). Furthermore, at the very early and late stages of the eclipse, there are no regions of totality within the penumbral region, and so the location and magnitude of the largest E_M value are not defined.

[79] To estimate E_M values within these regions, we apply the following algorithm. First, we locate the open end points of the penumbral perimeter at the terminator, compute the great circle distance and bearing angle between these points, and use those values to locate the midpoint. If there is no region of totality, we use this midpoint as the geographical location of maximum E_M , and set its value by interpolating linearly in time between the nearest time of total eclipse ($E_M = 1$) and the nearest time of zero eclipse ($E_M = 0$). Thus, at a point in time halfway between the times of first partial eclipse and first total eclipse, we set the maximum $E_M = 0.5$. To set all the other E_M values on the sphere, we first artificially close the penumbral perimeter by locating the point on the penumbral perimeter farthest away from this midpoint. Using the bearing angle between these two points, we locate another point in the opposite bearing direction located at a distance from this midpoint equal to the separation between the penumbral endpoints. This projected point always lies on the sphere within regions of negative $\cos \phi$ at an orientation roughly equal to the elliptical long axis of the eclipse shadow region. We then form lines from this projected point to both penumbral

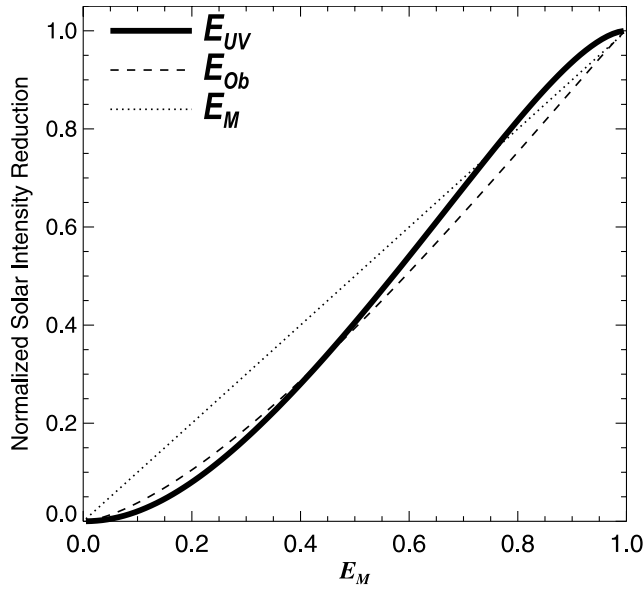


Figure A2. Plots as a function of E_M of eclipse magnitude E_M (dotted line), obscuration E_{Ob} (dashed line), and solar UV obscuration E_{UV} (thick solid line), for $(E_M)_{\max} = 1.02437$. See text for details.

endpoints using great circle projections, thereby creating an artificially closed penumbral perimeter. We then set all E_M values within this (now closed) perimeter using linear interpolation between the maximum E_M value (either at the umbral location or at the midpoint) and all points on this perimeter.

[80] With E_M values on the sphere now set, we use them to specify the reduction in solar UV irradiance. For this, the more pertinent parameter is the fraction of the surface area of the solar disk obscured by the Moon, known as the eclipse obscuration [Esenak and Anderson, 2001], and given by

$$E_{Ob} = \frac{A_{Ob}}{\pi R_S^2}, \quad (\text{A2})$$

where A_{Ob} is the surface area of the solar disk obscured by the Moon, shaded dark gray in Figure A1. For $0 \leq E_M \leq 1$, trigonometric manipulation using the geometry in Figure A1 yields the following analytical expressions:

$$\pi E_{Ob} = 2 \left(\frac{D_L}{D_S} \right)^2 \phi + \psi - \chi \sin \psi, \quad (\text{A3})$$

$$\chi = 1 + \frac{D_L}{D_S} - 2E_M = 2(E_M)_{\max} - 2E_M, \quad (\text{A4})$$

$$\phi = 2 \arcsin \left[\left\{ \left(\frac{D_S}{D_L} \right) \frac{E_M(1 - E_M)}{\chi} \right\}^{1/2} \right], \quad (\text{A5})$$

$$\psi = 2 \arcsin \left[\left\{ \left(\frac{D_L}{D_S} - E_M \right) \frac{E_M}{\chi} \right\}^{1/2} \right]. \quad (\text{A6})$$

The dotted and dashed lines in Figure A2 compare E_M and E_{Ob} , respectively, for $(E_M)_{\max} = 1.02437$.

[81] If solar irradiance was uniform across the solar disk, E_{Ob} could be used to scale down the solar constant S_0 in the model within the eclipse shadow as

$$S = S_0(1 - E_{Ob}). \quad (\text{A7})$$

While this is a fair approximation in the near-infrared, at shorter wavelengths solar intensities are brighter at the disk center and dimmer near the limb. Furthermore, the magnitude of this systematic center-to-limb decrease in solar intensities increases as wavelengths decrease down through the visible and into the mid-UV [e.g., Neckel, 2005]. Given this wavelength dependence, to simplify things we assume here that the dominant radiative heating influence occurs in the middle atmosphere at solar wavelengths 200–320 nm because of ozone absorption in the Hartley and Huggins bands.

[82] Observational specifications of solar limb darkening generally come as profiles of center-to-limb intensity variations of the normalized form

$$\hat{I}(\lambda, \mu) = \frac{I(\lambda, \mu)}{I(\lambda, 1)}, \quad (\text{A8})$$

where $I(\lambda, \mu)$ is the solar intensity at wavelength λ at a position $\mu = \cos \theta$ on the solar disk, and θ is the heliocentric angle: this coordinate is related to the radial distance R from the center of the solar disk as $R = R_S \sin \theta$. Here, we average

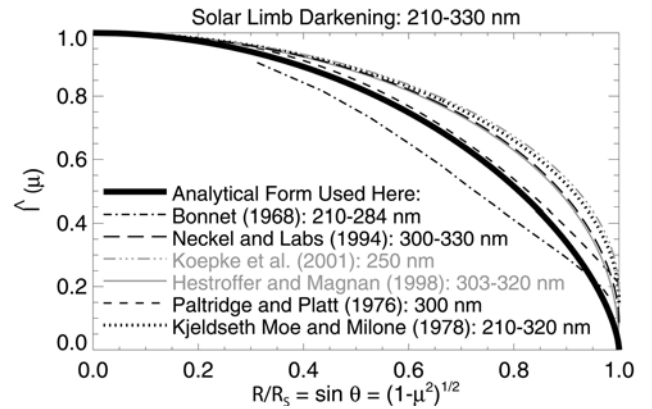


Figure A3. Solar limb darkening profiles $\hat{I}_{\lambda}(\mu)$, averaged over the wavelength ranges λ indicated, versus normalized solar disk radius $(1 - \mu^2)^{1/2}$, from the following sources: black dot-dashed curve, observations from Bonnet [1968, Table II]; black long-dashed curve, fits to observations from Neckel and Labs [1994, Table 1]; gray dot-dashed curve, Koepke et al. [2001, equations (2.1) and (2.2)]; gray solid curve, fits to observations using Hestroffer and Magnan [1998, equations (1) and (5)]; black short-dashed curve, Paltridge and Platt [1976, equation (3.1)]; black dotted curve, fits to observations from Kjeldseth Moe and Milone [1978, Table 3]. Thick black curve shows the analytical $\mu^{1.3}$ curve that we adopt in this study.

individual profiles over some band of UV wavelengths $\bar{\lambda} = [\lambda_1, \lambda_2]$ to yield a mean limb-darkening profile

$$\hat{I}_{\bar{\lambda}}(\mu) = \frac{1}{\lambda_2 - \lambda_1} \int_{\lambda_1}^{\lambda_2} \hat{I}(\lambda, \mu) d\lambda. \quad (\text{A9})$$

[83] Figure A3 plots $\hat{I}_{\bar{\lambda}}(\mu)$ from various published sources, with our $\bar{\lambda}$ range for each curve quoted in the bottom left of the plot. Limb darkening observations in the 200–320 nm band are quite limited. The most complete measurements shown in Figure A3 are those of *Bonnet* [1968] and *Kjeldseth Moe and Milone* [1978], which differ somewhat. *Greve and Neckel* [1996] reviewed these and other observations at 200–330 nm. Using the ratio of the disk-integrated to disk-center intensities

$$\frac{F}{I_C} = \frac{F(\lambda)}{I(\lambda, 1)} = \int_0^1 \mu \hat{I}(\lambda, \mu) d\mu, \quad (\text{A10})$$

Greve and Neckel [1996] argued that the *Kjeldseth Moe and Milone* [1978] data underestimate the limb darkening (F/I_C too large), whereas the *Bonnet* [1968] data fall toward the low end of the F/I_C range (see their Figure 1). On the basis of their analysis, we choose an $\hat{I}_{\bar{\lambda}}(\mu)$ profile of the form $\mu^{1.3}$, plotted in Figure A3, that lies midway between these two limiting profiles. This choice yields $F/I_C = 0.607$, a value within the range of the data given by *Greve and Neckel* [1996, Figure 1]. This profile specifies the two-dimensional limb darkening over the solar disk as

$$\begin{aligned} \hat{I}_{SD}(R, \varphi) &= \hat{I}_{\bar{\lambda}} \left(\left\{ 1 - [R/R_S]^2 \right\}^{1/2} \right), \\ &= \left(1 - [R/R_S]^2 \right)^{0.65}, \end{aligned} \quad (\text{A11})$$

where $\varphi = \arctan(Y/X)$ and $R = (X^2 + Y^2)^{1/2}$. These limb darkening contours are displayed on the solar disk in Figure A1.

[84] For a given eclipse magnitude E_M and obscuration E_{Ob} (A_{Ob}), we compute a corresponding obscuration of solar UV intensity as

$$E_{UV} = \frac{\int_{A_{Ob}} \hat{I}_{SD}(R, \varphi) dR d\varphi}{\int_0^{R_S} \int_0^{2\pi} \hat{I}_{SD}(R, \varphi) dR d\varphi}, \quad (\text{A12})$$

where the integration in the numerator is performed over the obscured surface area A_{Ob} . We evaluate equation (A12) numerically for the range of eclipse magnitudes E_M . The resulting $E_{UV}(E_M)$ curve is plotted in Figure A3. We use this curve to convert our E_M values into E_{UV} values for use in NOGAPS-ALPHA. These E_{UV} values are plotted as the white contours in Figure 1.

Appendix B: Fourier Solution of *Fritts and Luo* [1993] Equations

[85] From the starting equations (3)–(7), *Fritts and Luo* [1993] obtain relations for each independent variable, e.g.,

$$Lu^* = -(\alpha - N^2/g)F_x^*, \quad (\text{B1})$$

where $u^* = u(\bar{\rho}/\rho_0)^{1/2}$, $F^* = F(\bar{\rho}/\rho_0)^{1/2}g/(\bar{V}^2\bar{\theta})$,

$$L = \left(\alpha\beta + \frac{N^2}{\bar{V}^2} \right) \partial_x^2 + \left(\frac{N^2}{\bar{V}^2} \right) \partial_y^2, \quad (\text{B2})$$

$\alpha = \partial_z - \Gamma$, $\beta = \partial_z + \Gamma$, and $\Gamma = \bar{\rho}_z/(2\bar{\rho}) + g/c_s^2$ is Eckart's coefficient.

[86] To solve (B1), *Fritts and Luo* [1993] apply a Fourier transform in y and a sine transform in x . This leaves an inhomogeneous ordinary differential equation in z , expressed by their equation (19), which they solve numerically with the aid of a Green's function.

[87] Here we use a computationally faster approach based on a method developed by *Lighthill* [1960, 1978]. A three-dimensional Fourier transform is applied to (B1) to obtain

$$B\tilde{u}^* = -ik \left(\alpha - \frac{N^2}{g} \right) \tilde{F}^*. \quad (\text{B3})$$

Here \tilde{u}^* , u^* (and \tilde{F}^* , F^*) are Fourier-transform pairs:

$$u^*(x, y, z) = \int_{-\infty}^{\infty} \int_{-\infty}^{\infty} \tilde{u}^*(k, l, m) e^{i(kx+ly+mz)} dk dl dm. \quad (\text{B4})$$

[88] The term B in (B3) is obtained from L by replacing ∂_x , ∂_y , ∂_z with ik , il , im , respectively, giving

$$B = \left(m^2 + \Gamma^2 - \frac{N^2}{\bar{V}^2} \right) k^2 - \left(\frac{N^2}{\bar{V}^2} \right) l^2. \quad (\text{B5})$$

The gravity-wave dispersion relation is $B = 0$, which can be written as

$$m^2 = \frac{(k^2 + l^2)N^2}{\hat{\omega}^2} - \Gamma^2, \quad (\text{B6})$$

where $\hat{\omega} = -k\bar{V}$ is the intrinsic frequency. Note that the appearance of Γ^2 instead of the more usual $(\bar{\rho}_z/2\bar{\rho})^2 = \Gamma^2 + N^2/c_s^2$ in (B6) is a by-product of the use of the pseudo-incompressible rather than the fully compressible equations [cf. *Durrant*, 1989, equations (42) and (43)].

[89] Dividing (B3) by B and substituting into (B4) yields the spatial solution

$$u^* = \int_{-\infty}^{\infty} \int_{-\infty}^{\infty} \int_{-\infty}^{\infty} -ik \left(\alpha - \frac{N^2}{g} \right) \frac{\tilde{F}}{B} e^{i(kx+ly+mz)} dk dl dm. \quad (\text{B7})$$

Poles in the integrand occur where $B = 0$, so the integration with respect to m can be performed using the method of residues to obtain

$$u^* = 2\pi i \int_{-\infty}^{\infty} \int_{-\infty}^{\infty} -ik \left(\alpha - \frac{N^2}{g} \right) \frac{\tilde{F} e^{imz}}{B_m} e^{i(kx+ly)} dk dl, \quad (\text{B8})$$

where $B_m = 2k^2m$, and m is now treated as a function of k , l through (B6). *Lighthill* [1960, 1978] makes further analytical progress by using the stationary phase method, but this

involves a far-field approximation with an unspecified region of validity that is probably too restrictive for our purposes. Hence we approximate (B8) numerically using a fast Fourier transform.

[90] **Acknowledgments.** This work was supported in part by (1) NASA's Geospace Sciences Program, (2) a grant of computer time from the DoD High Performance Computing Modernization Program at the U.S. Army Space and Missile Defense Command Simulation Center, and (3) the Office of Naval Research. Funding for D.B. was provided by NSF grants ATM-0435789 and ATM-0448888. We thank D. E. Siskind for providing the CHEM1D night-to-day ratio in Figure 3b and A. Greve, H. Neckel, and two anonymous reviewers for their comments.

References

- Allen, D. R., L. Coy, S. D. Eckermann, J. P. McCormack, G. L. Manney, T. F. Hogan, and Y.-J. Kim (2006), NOGAPS-ALPHA simulations of the 2002 Southern Hemisphere stratospheric major warming, *Mon. Weather Rev.*, **134**, 498–518.
- Alpers, M., R. Eixmann, C. Fricke-Begemann, M. Gerding, and J. Höffner (2004), Temperature lidar measurements from 1 to 105 km altitude using resonance, Rayleigh, and rotational Raman scattering, *Atmos. Chem. Phys.*, **4**, 793–800.
- Altadil, D., J. G. Solé, and E. M. Apostolov (2001), Vertical structure of a gravity wave like oscillation in the ionosphere generated by the solar eclipse of August 11, 1999, *J. Geophys. Res.*, **106**, 21,419–21,428.
- Anderson, R. C., and D. R. Keefer (1975), Observation of the temperature and pressure changes during the 30 June 1973 solar eclipse, *J. Atmos. Sci.*, **32**, 228–231.
- Anderson, R. C., D. R. Keefer, and O. E. Myers (1972), Atmospheric pressure and temperature changes during the 7 March 1970 solar eclipse, *J. Atmos. Sci.*, **29**, 583–587.
- Aplin, K. R., and R. G. Harrison (2003), Meteorological effects of the eclipse of 11 August 1999 in cloudy and clear conditions, *Proc. R. Soc. London, Ser. A*, **459**, 353–371.
- Arendt, P. R. (1972), Ionospheric undulations during solar eclipse of 7 March 1970, *J. Atmos. Terr. Phys.*, **34**, 719–725.
- Ball, S. M., T. J. Stubbs, and R. A. Vincent (1980), Upper atmosphere wind observations over southern Australia during the total solar eclipse of 23 October 1976, *J. Atmos. Terr. Phys.*, **42**, 21–25.
- Ballard, H. N., R. Valenzuela, M. Izquierdo, J. S. Randhawa, R. Morla, and J. F. Bettel (1969), Solar eclipse: Temperature, wind and ozone in the stratosphere, *J. Geophys. Res.*, **74**, 711–712.
- Barker, E. (1992), Design of the Navy's multivariate optimum interpolation analysis system, *Weather Forecasting*, **7**, 220–231.
- Bertin, F., K. A. Hughes, and L. Kersley (1977), Atmospheric waves induced by the solar eclipse of 30 June 1973, *J. Atmos. Terr. Phys.*, **39**, 457–461.
- Boitman, O. N., A. D. Kalikhman, and A. V. Tashchilin (1999), The mid-latitude ionosphere during the total eclipse of March 9, 1997, *J. Geophys. Res.*, **104**, 28,197–28,206.
- Bonnet, R. (1968), Recherches sur l'émission continue du soleil entre 1950 et 3000 Å, *Ann. Astrophys.*, **31**, 597–634.
- Chimonas, G. (1970), Internal gravity-wave motions induced in the Earth's atmosphere by a solar eclipse, *J. Geophys. Res.*, **75**, 5545–5551.
- Chimonas, G. (1973), Lamb waves generated by the 1970 solar eclipse, *Planet. Space Sci.*, **21**, 1843–1854.
- Chimonas, G., and C. O. Hines (1970), Atmospheric gravity waves induced by a solar eclipse, *J. Geophys. Res.*, **75**, 875.
- Chimonas, G., and C. O. Hines (1971), Atmospheric gravity waves induced by a solar eclipse, **2**, *J. Geophys. Res.*, **76**, 7003–7005.
- Chou, M.-D., and M. J. Suarez (1999), A solar radiation parameterization for atmospheric studies, *NASA Tech. Memo. NASA/TM-1999-104606*, vol. 15, *Technical Report Series on Global Modeling and Data Assimilation*, edited by M. J. Suarez, 40 pp. (Available at <http://ntrs.nasa.gov>)
- Chou, M.-D., M. J. Suarez, X.-Z. Liang, and M. M.-H. Yan (2001), A thermal infrared radiation parameterization for atmospheric studies, *NASA Tech. Memo. NASA/TM-2001-104606*, vol. 19, *Technical Report Series on Global Modeling and Data Assimilation*, edited by M. J. Suarez, 56 pp. (Available at <http://ntrs.nasa.gov>)
- Connor, B. J., D. E. Siskind, J. J. Tsou, A. Parish, and E. E. Remsberg (1994), Ground-based microwave observations of ozone in the upper stratosphere and mesosphere, *J. Geophys. Res.*, **99**, 16,757–16,770.
- Davies, K. (1982), Atmospheric gravity waves induced by a solar eclipse—A review, *Proc. Indian Natl. Acad.*, **48A**, 342–355.
- Davies, T., A. Staniforth, N. Wood, and J. Thurnburn (2003), Validity of anelastic and other equation sets as inferred from normal-mode analysis, *Q. J. R. Meteorol. Soc.*, **129**, 2761–2775.
- Davis, M. J., and A. V. da Rosa (1970), Possible detection of atmospheric gravity waves generated by a solar eclipse, *Nature*, **226**, 1123.
- Durrant, D. R. (1989), Improving the anelastic approximation, *J. Atmos. Sci.*, **46**, 1453–1461.
- Eaton, F. D., J. R. Hines, W. H. Hatch, R. M. Cionco, J. Byers, D. Garvey, and D. R. Miller (1997), Solar eclipse effects observed in the planetary boundary layer over a desert, *Boundary Layer Meteorol.*, **83**, 331–346.
- Eckermann, S. D., I. Hirota, and W. K. Hocking (1995), Gravity-wave and equatorial-wave morphology of the stratosphere derived from long-term rocket soundings, *Q. J. R. Meteorol. Soc.*, **121**, 149–186.
- Eckermann, S. D., J. P. McCormack, L. Coy, D. R. Allen, T. F. Logan, and Y.-J. Kim (2004), NOGAPS-ALPHA: A prototype high-altitude global NWP model, paper presented at Symposium on the 50th Anniversary of Operational Numerical Weather Prediction, Am. Meteorol. Soc., Univ. of Md., College Park, 14–17 June. (Available at http://uap-www.nrl.navy.mil/dynamics/papers/Eckermann_P2.6-reprint.pdf)
- Errico, R. M., E. H. Barker, and R. Gelaro (1988), A determination of balanced normal modes for two models, *Mon. Weather Rev.*, **116**, 2717–2724.
- Espenak, F., and J. Anderson (2001), Total solar eclipse of 2002 December 04, *NASA Tech. Pap. NASA/TP-2001-209990*, 77 pp. (Available at <http://umbra.nascom.nasa.gov/eclipse/021204/rp.html>)
- Farges, T., A. Le Pichon, E. Blanc, S. Perez, and B. Alcoverro (2003), Response of the lower atmosphere and ionosphere to the eclipse of August 11, 1999, *J. Atmos. Sol. Terr. Phys.*, **65**, 717–726.
- Fleming, E. L., S. Chandra, J. J. Barnett, and M. J. Corney (1990), Zonal mean temperature, pressure, zonal wind, and geopotential height as functions of latitude, COSPAR International Reference Atmosphere: 1986, part II: Middle Atmosphere Models, *Adv. Space Res.*, **10**(12), 11–59.
- Fortuin, J. P. F., and H. Kelder (1998), An ozonesonde climatology based on ozonesonde and satellite measurements, *J. Geophys. Res.*, **103**, 31,709–31,734.
- Fritts, D. C., and Z. Luo (1993), Gravity wave forcing in the middle atmosphere due to reduced ozone heating during a solar eclipse, *J. Geophys. Res.*, **98**, 3011–3021.
- Frost, A. D., and R. R. Clark (1973), Predicted acoustic gravity wave enhancement during the solar eclipse of June 30, 1973, *J. Geophys. Res.*, **78**, 3995–3997.
- Goerrs, J. S., and P. A. Phoebus (1992), The Navy's operational atmospheric analysis, *Weather Forecasting*, **7**, 232–249.
- Goodwin, G. L., and G. J. Hobson (1978), Atmospheric gravity waves generated during a solar eclipse, *Nature*, **275**, 109–111.
- Greve, A., and H. Neckel (1996), On the consistency of solar limb darkening observations at UV wavelengths (2000–3300 Å), *Astron. Astrophys. Suppl. Ser.*, **120**, 35–39.
- Grooss, J.-U., and J. M. Russell III (2005), Technical note: A stratospheric climatology for O₃, H₂O, CH₄, NO_x, HCl and HF derived from HALOE measurements, *Atmos. Chem. Phys.*, **5**, 2797–2807.
- Gross, P., and A. Hense (1999), Effects of a total solar eclipse on the mesoscale atmospheric circulation over Europe—A model experiment, *Meteorol. Atmos. Phys.*, **71**, 229–242.
- Hanuis, C., P. Broche, and G. Ogubazghi (1982), HF Doppler observations of gravity waves during the 16 February 1980 solar eclipse, *J. Atmos. Terr. Phys.*, **44**, 963–966.
- Hestroffer, D., and C. Magnan (1998), Wavelength dependency of the solar limb darkening, *Astron. Astrophys.*, **333**, 338–342.
- Hogan, T. F., and T. E. Rosmond (1991), The description of the Navy Operational Global Atmospheric Prediction System's spectral forecast model, *Mon. Weather Rev.*, **119**, 1786–1815.
- Holton, J. R., J. H. Beres, and X. Zhou (2002), On the vertical scale of gravity waves excited by localized thermal forcing, *J. Atmos. Sci.*, **59**, 2019–2023.
- Hunt, B. G. (1965), A theoretical study of the changes occurring in the ozonosphere during a total eclipse of the sun, *Tellus*, **17**, 516–523.
- Hunter, A. N., B. K. Holman, D. G. Feldgate, and R. Kelleher (1974), Faraday rotation studies in Africa during the solar eclipse of June 30, 1973, *Nature*, **250**, 205–206.
- Jackson, D. R., S. J. Driscoll, E. J. Highwood, J. E. Harries, and J. M. Russell (1998), Troposphere to stratosphere transport at low latitudes as studied using HALOE observations of water vapour 1992–1997, *Q. J. R. Meteorol. Soc.*, **124**, 169–192.
- Jerlov, N., H. Olson, and W. Schuepp (1954), Measurements of solar radiation at Loevangerin Sweden during the total eclipse 1945, *Tellus*, **6**, 44–45.
- Jones, B. W. (1976), A search for Lamb waves generated by the solar eclipse of 11 May 1975, *J. Atmos. Sci.*, **33**, 1820–1823.
- Jones, B. W. (1999), A search for atmospheric pressure waves from the total solar eclipse of 9 March 1997, *J. Atmos. Sol. Terr. Phys.*, **61**, 1017–1024.
- Jones, B. W., and R. S. Bogart (1975), Eclipse induced atmospheric gravity waves, *J. Atmos. Terr. Phys.*, **37**, 1223–1226.

- Jones, B. W., G. J. Miseldine, and R. J. A. Lambourne (1992), A possible atmospheric pressure wave from the total solar eclipse of 22 July 1990, *J. Atmos. Terr. Phys.*, **54**, 113–115.
- Jones, T. B., D. M. Wright, J. Milner, T. K. Yeoman, T. Reid, P. J. Chapman, and A. Senior (2004), The detection of atmospheric waves produced by the total solar eclipse of 11 August 1999, *J. Atmos. Terr. Phys.*, **66**, 363–374.
- Kasahara, A., and J.-H. Qian (2000), Normal modes of a global nonhydrostatic model, *Mon. Weather Rev.*, **128**, 3357–3375.
- Kaufmann, M., O. A. Gusev, K. U. Grossman, F. J. Martin-Torres, D. R. Marsh, and A. A. Kutepov (2003), Satellite observations of daytime and nighttime ozone in the mesosphere and lower thermosphere, *J. Geophys. Res.*, **108**(D9), 4272, doi:10.1029/2002JD002800.
- Kawabata, Y. (1937), Spectrographic observation of the amount of ozone at the total solar eclipse of June 19, 1936, *J. Astron. Geophys.*, **14**, 1–3.
- Kjeldseth Moe, O., and E. F. Milone (1978), Limb darkening 1945–3245 A for the quiet Sun from Skylab data, *Astrophys. J.*, **226**, 301–314.
- Koepke, P., J. Reuder, and J. Schween (2001), Spectral variation of the solar radiation during an eclipse, *Meteorol. Z.*, **10**, 179–196.
- Li, D., and K. P. Shine (1995), A 4-dimensional ozone climatology for UGAMP models, *UGAMP Internal Rep.* 35, 35 pp., Cent. for Global and Atmos. Modell., Dep. of Meteorol., Univ. of Reading, Reading, U. K.
- Lighthill, M. J. (1960), Studies on magnetohydrodynamic waves and other anisotropic wave motions, *Philos. Trans. R. Soc. London, Ser. A*, **252**, 397–430.
- Lighthill, M. J. (1978), *Waves in Fluids*, 504 pp., Cambridge Univ. Press, New York.
- Lindzen, R. S., and D. Blake (1972), Lamb waves in the presence of realistic distributions of temperature and dissipation, *J. Geophys. Res.*, **77**, 2166–2176.
- López-Puertas, M., and F. W. Taylor (2001), *Non-LTE Radiative Transfer in the Atmosphere*, 487 pp., World Sci., Singapore.
- Marks, C. J., and S. D. Eckermann (1995), A three-dimensional nonhydrostatic ray-tracing model for gravity waves: Formulation and preliminary results for the middle atmosphere, *J. Atmos. Sci.*, **52**, 1959–1984.
- McCormack, J. P., and D. E. Siskind (2002), Simulations of the quasi-biennial oscillation and its effect on stratospheric H₂O, CH₄, and age of air with an interactive two-dimensional model, *J. Geophys. Res.*, **107**(D22), 4625, doi:10.1029/2002JD002141.
- McCormack, J. P., et al. (2004), NOGAPS-ALPHA model simulations of stratospheric ozone during the SOLVE2 campaign, *Atmos. Chem. Phys.*, **4**, 2401–2423.
- McIntosh, B. A., and D. O. Revelle (1984), Traveling atmospheric pressure waves measured during a solar eclipse, *J. Geophys. Res.*, **89**, 4953–4962.
- Müller-Wodarg, I. C. F., A. D. Aylward, and M. Lockwood (1998), Effects of a mid-latitude solar eclipse on the thermosphere and ionosphere: A modelling study, *Geophys. Res. Lett.*, **25**, 3787–3790.
- Murgatroyd, R. J., and R. M. Goody (1958), Sources and sinks of radiative energy from 30 to 90 km, *Q. J. R. Meteorol. Soc.*, **84**, 225–234.
- Neckel, H. (2005), Analytical reference functions $F(\lambda)$ for the Sun's limb darkening and its absolute continuum intensities, *Sol. Phys.*, **229**, 13–33.
- Neckel, H., and D. Labs (1994), Solar limb darkening 1986–1990 (λ 303 to 1099 nm), *Sol. Phys.*, **153**, 91–114.
- Paltridge, G. W., and C. M. R. Platt (1976), *Radiative Processes in Meteorology and Climate*, 318 pp., Elsevier, Amsterdam.
- Prenosil, T. (2000), The influence of the 11 August 1999 total solar eclipse on the weather over central Europe, *Meteorol. Z.*, **9**, 351–359.
- Quiroz, R. S., and R. M. Henry (1973), Stratospheric cooling and perturbation of the meridional flow during the solar eclipse of 7 March 1970, *J. Atmos. Sci.*, **30**, 480–488.
- Randhawa, J. S. (1968), Mesospheric ozone measurements during a solar eclipse, *J. Geophys. Res.*, **73**, 493–495.
- Randhawa, J. S. (1973), An investigation of solar eclipse effect on the subpolar stratosphere, *J. Geophys. Res.*, **78**, 7139–7144.
- Randhawa, J. S. (1974), Partial solar eclipse effects on temperature and wind in an equatorial atmosphere, *J. Geophys. Res.*, **79**, 5052–5054.
- Ricard, P., J. de La Noë, B. J. Connor, L. Froidevaux, J. W. Waters, R. S. Harwood, I. A. MacKenzie, and G. E. Peckham (1996), Diurnal variability of mesospheric ozone as measured by the UARS microwave limb sounder instrument: Theoretical and ground-based validations, *J. Geophys. Res.*, **101**, 10,077–10,089.
- Ridley, E. C., R. E. Dickinson, R. G. Roble, and M. H. Rees (1984), Thermospheric response to the June 11, 1983, solar eclipse, *J. Geophys. Res.*, **89**, 7583–7588.
- Roble, R. G., B. A. Emery, and E. C. Ridley (1986), Ionospheric and thermospheric response over Millstone Hill to the May 30, 1984 annular solar eclipse, *J. Geophys. Res.*, **91**, 1661–1670.
- Salby, M. L., and R. R. Garcia (1987), Transient response to localized episodic heating in the tropics, part I, excitation and short-time near-field behavior, *J. Atmos. Sci.*, **44**, 458–498.
- Schmidlin, F. J., and R. O. Olsen (1984), Modification of the strato-mesospheric temperature and wind structure resulting from the 26 February 1979 solar eclipse, *J. Atmos. Terr. Phys.*, **46**, 273–280.
- Schödel, J. P., J. Klostermeyer, and J. Röttger (1973), Atmospheric gravity wave observations after the solar eclipse of June 30, 1973, *Nature*, **245**, 87–88.
- Sears, R. D. (1972), Ionospheric HF Doppler dispersion during the eclipse of 7 March 1970, *J. Atmos. Terr. Phys.*, **34**, 727–732.
- Segal, M., R. W. Turner, J. Prusa, R. J. Bitzer, and S. V. Finley (1996), Solar eclipse effect on shelter air temperature, *Bull. Am. Meteorol. Soc.*, **77**, 89–99.
- Seykora, E. J., A. Bhatnagar, R. M. Jain, and J. L. Streete (1985), Evidence of atmospheric gravity waves produced during the 11 June 1983 total solar eclipse, *Nature*, **313**, 124–125.
- Siskind, D. E., B. J. Connor, R. S. Eckman, E. E. Remsburg, J. J. Tsou, and A. Parrish (1995), An intercomparison of model ozone deficits in the upper stratosphere and mesosphere from two data sets, *J. Geophys. Res.*, **100**, 11,191–11,202.
- Stranz, D. (1961), Ozone measurements during solar eclipse, *Tellus*, **13**, 276–279.
- Swinbank, R., and D. A. Ortlund (2003), Compilation of wind data for the Upper Atmosphere Research Satellite (UARS) reference atmosphere project, *J. Geophys. Res.*, **108**(D19), 4615, doi:10.1029/2002JD003135.
- Vogel, B., M. Baldauf, and F. Fielder (2001), The influence of a solar eclipse on temperature and wind in the Upper-Rhine Valley—A numerical case study, *Meteorol. Z.*, **10**, 207–214.

D. Broutman and J. Ma, Computational Physics, Inc., 8001 Braddock Road, Springfield, VA 22151, USA.

S. D. Eckermann and J. P. McCormack, Space Science Division, Code 7646, Naval Research Laboratory, Washington, DC 20375, USA. (stephen.eckermann@nrl.navy.mil)

T. F. Hogan, Marine Meteorology Division, Code 7532, Naval Research Laboratory, Monterey, CA 93943, USA.

M. T. Stollberg, Astronomical Applications Department, U.S. Naval Observatory, Washington, DC 20392, USA.